The Astrophysical Journal, 970:169 (18pp), 2024 August 1 https://doi.org/10.3847/1538-4357/ad3df0

Primordial Black Hole Dark Matter Simulations Using PopSyCLE

Kerianne Pruett[1], William Dawson[1], Michael S. Medford[2,3], Jessica R. Lu[2], Casey Lam[2], Scott Perkins[1], Peter McGill[1], Nathan Golovich[1], and George Chapline[1]
[1] Lawrence Livermore National Laboratory, Livermore, CA 94550, USA; pruett6@llnl.gov
[2] Department of Astronomy, University of California, Berkeley, CA 94720, USA
[3] Lawrence Berkeley National Laboratory, Berkeley, CA 94720, USA
Received 2022 November 11; revised 2024 April 8; accepted 2024 April 10; published 2024 July 29

Abstract

Primordial black holes (PBHs), theorized to have originated in the early Universe, are speculated to be a viable form of dark matter. If they exist, they should be detectable through photometric and astrometric signals resulting from gravitational microlensing of stars in the Milky Way. Population Synthesis for Compact-object Lensing Events, or PopSyCLE, is a simulation code that enables users to simulate microlensing surveys, and is the first of its kind to include both photometric and astrometric microlensing effects, which are important for potential PBH detection and characterization. To estimate the number of observable PBH microlensing events, we modify PopSyCLE to include a dark matter halo consisting of PBHs. We detail our PBH population model, and demonstrate our PopSyCLE + PBH results through simulations of the Optical Gravitational Lensing Experiment-IV (OGLE-IV) and Nancy Grace Roman Space Telescope (Roman) microlensing surveys. We provide a proof-of-concept analysis for adding PBHs into PopSyCLE, and thus include many simplifying assumptions, such as $f_{\rm DM}$, the fraction of dark matter composed of PBHs, and $\bar{m}_{\rm PBH}$, mean PBH mass. Assuming $\bar{m}_{\rm PBH} = 30\ M_\odot$, we find $\sim 3.6 f_{\rm DM}$ times as many PBH microlensing events than stellar evolved black hole events, a PBH average peak Einstein crossing time of ∼91.5 days, estimate on order of $10^2 f_{\rm DM}$ PBH events within the 8 yr OGLE-IV results, and estimate Roman to detect $\sim 1000 f_{\rm DM}$ PBH microlensing events throughout its planned microlensing survey.

Unified Astronomy Thesaurus concepts: Primordial black holes (1292); Dark matter (353); Gravitational microlensing (672); Astrometric microlensing effect (2140); Microlensing parallax (2144); Microlensing event rate (2146); Astronomical simulations (1857); Astronomy software (1855)

1. Introduction

Approximately 85% of the matter in our Universe is composed of dark matter, which is not well understood. Dark matter cannot be observed via electromagnetic mechanisms (hence "dark") and is only observable through gravitational interactions, making it challenging to detect. Primordial black holes (PBHs), hypothesized in the 1960s (Zel'dovich & Novikov 1967), are a theoretical type of black hole (BH) believed to be a viable dark matter candidate. Unlike BHs, which are formed through stellar evolution, PBHs are thought to have formed in the early Universe (within seconds of the Big Bang; e.g., Carr & Silk 2018) via gravitational collapse in overdense regions. PBHs are theorized to have formed during the radiation-dominated era, before Big Bang nucleosynthesis, thus they are considered nonbaryonic and are speculated to behave like "cold" dark matter. Our current understanding of the Universe places a 5% constraint on the baryonic matter fraction (Collaboration et al. 2014), meaning that stellar evolved BHs can never account for more than 5% of the energy density in our Universe. Thus, while we know that stellar evolved BHs exist and may contribute to the dark matter fraction, we know they cannot explain the majority of the missing dark matter in our Universe.

Because PBHs formed at roughly the cosmological horizon (Chapline 1975a), their initial masses should correspond to the horizon mass:

$$M \sim \frac{c^3 t}{G},$$

where c is the speed of light, t is the time since the Big Bang, and G is the gravitational constant (Carr 1975; Carr & Kuhnel 2021). This means that PBHs should have masses between $\sim 10^{-8}$ kg (if formed at Planck time $t = 10^{-43}$ s) and $\sim 10^5\ M_\odot$ (if formed at $t = 1$ s; Carr 1975). PBHs are considered "free-floating" in the late Universe, and should retain roughly their initial masses (Chapline 1975a). The initial conjecture of PBHs drove Hawking (1971) to study the quantum-gravitational effects of BHs, and led to the discovery that PBHs formed before $t = 10^{-23}$ s ($M \sim 10^{12}$ kg) should have evaporated by the present day (Hawking 1974).

In 2016, the Laser Interferometer Gravitational-Wave Observatory (LIGO) detected gravitational waves from two merging $\sim 30\ M_\odot$ BHs (Abbott et al. 2016) that were potentially primordial in origin (Bird et al. 2016). The idea of PBHs as a viable form of dark matter had nearly died out over the last few decades due to insufficient new evidence or microlensing results (e.g., Alcock et al. 1993; Aubourg et al. 1993; Udalski et al. 1994; Wyrzykowski et al. 2011; Croon et al. 2020; and others); however, our inability to detect dark matter (of any variety) throughout that time, combined with recent scientific discoveries, has reinvigorated scientists to explore PBHs as a potential dark matter candidate. These recent explorations have placed very tight constraints on $f_{\rm DM}$ covering many decades in mass (see summary in Bird et al. 2023).

If PBHs exist, they should be present within our Milky Way galaxy (Chapline 1975b) and observable via gravitational microlensing signals from local stars (e.g., Chapline & Frampton 2016). Microlensing is the effect when a foreground object (the lens) passes in front of a luminous background object (the source), relative to the observer, in such a way that causes magnification of the source flux. While microlensing can cause magnification on the same order as strong gravitational lensing (i.e., multiple images), it happens on a smaller angular scale, such that lensed images are too small to be resolved.

Microlensing imparts a characteristic photometric signal on the measured light curves of lensed stars, which can be used to detect and characterize foreground objects irrespective of their luminosity or whether they are gravitationally bound to a companion. Unlike other probes, such as gravitational waves or X-ray binaries, microlensing can detect free-floating PBHs, in addition to binary BH systems, and enables us to infer properties of the lens without observing the lens itself. Because PBHs interact gravitationally and not electromagnetically, microlensing is the most direct means of probing PBHs.

The angular Einstein radius of a microlensing event, θ_E, sets the angular scale of the microlensing event, and is given by

$$\theta_E = \sqrt{\frac{4GM}{c^2}\left(\frac{1}{d_L} - \frac{1}{d_S}\right)}, \tag{1}$$

where d_S is the observer–source distance, and d_L is the observer–lens distance.

Microlensing parallax, π_E, causes asymmetries in the photometric light curve and is caused by differences in the relative location of the observer with respect to the source–lens axis, as can happen when Earth orbits the Sun during long duration events:

$$\pi_E = \frac{\pi_{\rm rel}}{\theta_E}, \tag{2}$$

where $\pi_{\rm rel}$ is the relative parallax:

$$\pi_{\rm rel} = 1{\rm au}\left(\frac{1}{d_L} - \frac{1}{d_S}\right).$$

The Einstein crossing time can then be determined using the magnitude of the relative source–lens proper motion, $\mu_{\rm rel}$:

$$t_E = \frac{\theta_E}{\mu_{\rm rel}},$$

which describes the characteristic timescale of the event (i.e., the time it takes for the source to transit the Einstein radius of the lens).

In addition to photometric measurements, one can obtain astrometric measurements for microlensing events using the location and movement of stars. In the absence of lensing and parallax a source star would appear to make a straight line on the sky over most observable timescales; however, in the presence of lensing, the source appears to shift nonlinearly throughout the duration of the microlensing event. Thus, by measuring the change in location of the source image centroid throughout the microlensing event, one can determine the astrometric shift, $\boldsymbol{\delta}_c$:

$$\boldsymbol{\delta}_c = \frac{\theta_E}{u^2 + 2}\boldsymbol{u}. \tag{3}$$

Then, using the angular on-sky positions of the source and lens (φ_S and φ_L, respectively), one can determine the source–lens separation vector:

$$\boldsymbol{u} = \frac{\varphi_S - \varphi_L}{\theta_E}.$$

By comparing the observed distribution of microlensing events to simulated distributions in π_E, t_E, $\bar{\delta}_c$, and $\mu_{\rm rel}$ space, both with and without PBHs, we can ultimately place constraints on PBH dark matter abundance in the Milky Way. We can then estimate expected statistical signatures for each population by simulating the stellar and dark matter components of the Milky Way, and can analyze the resulting microlensing properties after being filtered by a simulated observational survey.

In this work, we describe how `PopSyCLE` is used to generate a simulated microlensing survey in the Milky Way (Section 2), the steps used to inject PBHs into `PopSyCLE` (Section 3), and analysis on the resulting microlensing events (Section 4). As a proof of concept, we then consider our simulation results in the context of current and future surveys (Section 5).

2. PopSyCLE Pipeline

Population Synthesis Code for Compact Object Microlensing Events, or `PopSyCLE`, is a Python package that enables the user to simulate synthetic microlensing surveys in the Milky Way.[4] `PopSyCLE` is a resolved microlensing simulation code, and the first of its kind to include both photometric and astrometric microlensing signals, and numerically derived compact object models (Lam et al. 2020).

`PopSyCLE` relies on first using `Galaxia`[5] (Sharma et al. 2011) to generate a synthetic model of the Milky Way populated with stars, and `SPISEA`[6] (Hosek et al. 2020) to generate and inject compact objects into the Milky Way model. `PopSyCLE` then uses the resulting outputs to simulate a microlensing survey with user-specified parameters, enabling the user to control survey length, observing frequency, and various observational parameters. We briefly summarize these tools in the remainder of this section (additional detail in Lam et al. 2020).

2.1. Galaxia

`Galaxia` is first used to populate a stellar model of the Milky Way, using the Besançon analytic model (Robin et al. 2004). We adopt changes to the bulge kinematics (following the "v3" modifications from Lam et al. 2020, Appendix A) and reddening laws (Lam et al. 2020, Appendix B) in the standard `Galaxia` package in an attempt to eliminate discrepancies with observations, and to more accurately represent the event-rate predictions for the scope of this study.

For bulge kinematics, we modify the Milky Way parameters in `Galaxia` to use a pattern speed of $\Omega = 40$ km s^{-1} kpc^{-1}, a bulge velocity dispersion of $\sigma_R = \sigma_\phi = 100$ km s^{-1}, a bar angle

[4] https://github.com/jluastro/PopSyCLE
[5] http://galaxia.sourceforge.net
[6] https://github.com/astropy/SPISEA

of $\alpha = 28°$, and a bar length of $x_0 = 0.7$ kpc. The default `Galaxia` extinction maps are not accurate in the high-extinction regions of the inner bulge, so we modify our output in accordance to the reddening law from Damineli et al. (2016).

2.2. SPISEA

The Stellar Population Interface for Stellar Evolution and Atmospheres, or `SPISEA`, is a Python package used to generate star clusters (single-age and single-metallicity populations) using various input parameters, including age, mass, metallicity, extinction, atmospheric models, and initial mass functions (Hosek et al. 2020). `SPISEA` allows for compact object generation by supporting user control of the initial–final mass relation (IFMR; Rose et al. 2022). We follow the `SPISEA` modifications outlined in Lam et al. (2020) Section 2.2, which uses the `Raithel18` (Raithel et al. 2018) IFMR from recent simulations, along with the zero-age main-sequence (ZAMS) mass of each star, in order to build a population of stellar evolved BHs, neutron stars (NSs), and white dwarfs (WDs).

2.3. PopSyCLE

`Galaxia` assigns objects to four populations: thin disk (150 Myr–10 Gyr), bulge (10 Gyr), thick disk (11 Gyr), and stellar halo (14 Gyr). `PopSyCLE` then splits the thin-disk population into 29 age bins and changes the age of the stellar halo population to 13.8 Gyr (Lam et al. 2020, Section 3).

Once `SPISEA` has generated the compact objects,[7] they get injected back into the stellar population.[8] Following Lam et al. (2020), we assign initial "kick" velocities (in addition to stellar velocities) to NSs and BHs, assigning values of 350 km s^{-1} and 100 km s^{-1}, respectively. Compact objects' (BHs, WDs, NSs) position and velocity follow that of the stellar population in `Galaxia`, and are considered "dark" sources (with the exception of luminous WDs; Lam et al. 2020).

Microlensing events are assumed to be "point source, point lens" (meaning both the source and lens are treated as point sources), and event calculation follows that described in Lam et al. (2020, Section 4). Initial event candidates are determined using a cut on the separation between each object and its nearest on-sky neighbor, $\Delta\theta \leqslant \theta_{\rm blend}$, in which $\theta_{\rm blend}$ is the survey-specific seeing-disk radius, and defines the angular projected distance from the lens in which objects are considered blended.

Event detectability is determined by calculating the Einstein radius, θ_E, following Equation (1). The list of candidates is then narrowed down to contain only those events which satisfy the following equation:

$$\frac{\Delta\theta}{\theta_E} < u_{0,\rm max},$$

where $u_{0,\rm max}$ is the impact parameter threshold for the survey. Events are then cut again to ensure that they satisfy the user-specified selection criteria, related to the survey duration and cadence. Lastly, events with dark objects as sources are removed, as they are nonobservable events. Every event candidate remaining is considered an event in the simulation and the user is left with catalogs containing photometric and astrometric microlensing parameters for each event.

Table 1
PBH Simulation Parameters

Parameter	Description	Value
$\bar{m}_{\rm PBH}$	Mean PBH mass	30 $M_\odot$
$f_{\rm DM}$	PBH dark matter fraction	1.0
$v_{\rm esc}$	Milky Way escape velocity	550 km s^{-1}
ρ_0	Characteristic density of Milky Way dark matter halo	0.0093 $M_\odot$ pc^{-3}
r_s	Scale radius of Milky Way dark matter halo	18.6 kpc
r_{gc}	Distance between the Sun and Galactic center	8.3 kpc
$r_{\rm max}$	Max distance from Earth to populate PBHs ($2 \times r_{gc}$)	16.6 kpc
γ	Milky Way Halo inner slope	1, 0.5, or 0.25

3. Primordial Black Hole Injection

Before this work, `PopSyCLE` supported the compact object populations of NSs, WDs, and BHs, but had no implementation for PBHs. We update `PopSyCLE` to include the addition of an optional PBH population using the parameters and assumptions given in Table 1.[9]

Including a PBH population in `PopSyCLE` requires injecting PBHs into our projected survey line of sight (LOS) by first determining how many PBHs to simulate for the given field (detailed in Section 3.2). PBHs have spatial and velocity distributions following that of the dark matter halo, rather than the distributions for stellar remnant compact objects which were born in the Galactic disk. For this reason, we then have to assign positions (detailed in Section 3.3) and velocities (detailed in Section 3.4) to each PBH based on the halo density and speed profiles. Three-dimensional positions and velocities are assigned by sampling the radial components (with respect to the Galactic center) from the relevant distributions, and randomly sampling the angular components over the possible ranges. Once a PBH population for a given field has been generated, we inject the objects into the synthetic Milky Way generated from `Galaxia` and `SPISEA`, thus enabling `PopSyCLE` to simulate a microlensing survey with PBHs present.

3.1. PBH Distribution

We assume that Milky Way dark matter follows the halo density profile in McMillan (2016):

$$\rho(r) = \frac{\rho_0}{\left(\frac{r}{r_s}\right)^{\gamma}\left(1 + \frac{r}{r_s}\right)^{(3-\gamma)}}, \quad (4)$$

where r is the distance from the Galactic center (in the galactocentric coordinate frame), γ is the halo inner density slope, r_s is the scale radius of the halo, and ρ_0 is the halo characteristic density. An inner slope of $\gamma = 1$ corresponds to the Navarro–Frenk–White (NFW) profile (Navarro et al. 1996), and is used for all simulation results in this work (though `PopSyCLE + PBH` supports γ values of 1, 0.5, and 0.25). The

[7] We use `PopSyCLE` at commit `#018af97`, which considers only singular stars and compact objects.

[8] `PopSyCLE` is being updated to support binary populations, updated IFMRs, and a NS mass spectrum, however these updates are not reflected in the results of this work.

[9] https://github.com/jluastro/PopSyCLE/tree/pbh

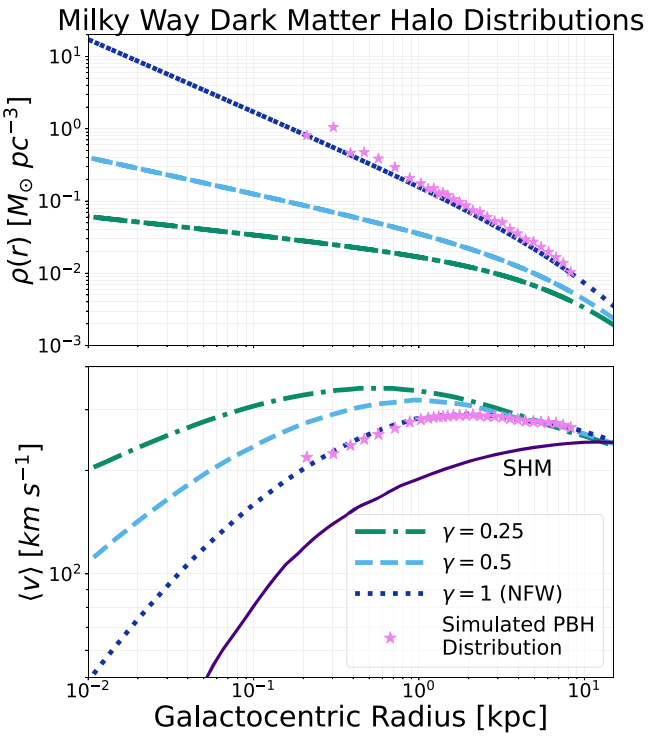

Figure 1. Upper: halo density as a function of radius, for varying halo inner density slopes. Lower: a recreation of the Eddington inversion curves from Figure 11 of Lacroix et al. (2018), demonstrating how the mean speed profile changes as a function of inner slope. The standard halo model is shown by the solid line. In both panels the stars show that the injected PBHs trace the intended profiles.

upper panel of Figure 1 demonstrates how the halo density changes as a function of radius and γ. We choose $r_{gc} = 8.3$ kpc to be the distance between the Sun and Galactic center (which is typical of the literature; e.g., Gillessen et al. 2009; Chatzopoulos et al. 2015), $r_s = 18.6$ kpc to be the halo scale radius, $\rho_0 = 0.0093$ $M_\odot$ pc^{-3} to be the halo characteristic density (which are the median r_s and ρ_0 values determined by McMillan 2016, given their mass model), and $r_{\max} \equiv 2\ r_{gc}$ to be the maximum galactocentric radius (toward the Galactic center) to populate objects out to (as we do not expect to detect a significant number of microlensing events beyond that).

3.2. PBH Number

To determine the number of PBHs to include in a given simulation, we first construct a LOS extending from $r = 0$ (the Sun) to the center of the field being simulated (l and b, at a heliocentric distance of $r = r_{\max}$). We then assume that PBHs will populate a heliocentric LOS cylinder (shown in Figure 2, described in Section 3.3) whose center axis is the LOS and radius, R, corresponds to the projected survey radius at the distance $r_{\max}$ (see Figure 2). Next, we split the LOS into 100,000 equally spaced points for numerically integrating the LOS dark matter density (accounting for galactocentric to LOS coordinate transformations), enabling us to approximate the total mass within the LOS cylinder, $M_{\rm LOS}$.[10]

Using the fraction of dark matter composed of PBHs, $f_{\rm DM}$, and mean PBH mass, $\bar{m}_{\rm PBH}$, we can then determine the number of PBHs to inject in a given field, $N_{\rm PBH}$:

$$N_{\rm PBH} = f_{\rm DM}\left(\frac{M_{\rm LOS}}{\bar{m}_{\rm PBH}}\right). \quad (5)$$

For the scope of this work, we assume $f_{\rm DM} = 1$ and assign PBHs a monochromatic mass of $\bar{m}_{\rm PBH} = 30\ M_\odot$, as we find this to be roughly consistent with inferred masses of LIGO-detected BHs (e.g., Abbott et al. 2016, 2017a, 2017b; Lu et al. 2019). We acknowledge that these assumptions contradict existing $f_{\rm DM}$ constraints (e.g., Alcock et al. 2001; Tisserand et al. 2007; Wyrzykowski et al. 2011; Blaineau et al. 2022), and expectations of an extended mass distribution (e.g., Chapline 1975a, 1975b; Carr 1975; Chapline & Frampton 2016; Carr & Silk 2018; Chapline & Barbieri 2018; Carr & Kuhnel 2021); however, our primary focus is on demonstrating the addition of a PBH population into the `PopSyCLE` simulation code. For this reason, we believe these choices are acceptable, as they enable readers to easily transform the results to other values of $f_{\rm DM}$ and $\bar{m}_{\rm PBH}$, while reducing Poisson noise.

3.3. PBH Positions

After determining the number of PBHs that should be simulated within the LOS for a given field, $N_{\rm PBH}$, we assign each PBH a distance along the LOS, r, using inverse transform sampling (e.g., Press et al. 1988) to assign each PBH a galactocentric radius based on a numerical approximation of the cumulative distribution function of the normalized dark matter density function. Each PBH galactocentric radius is then converted to a heliocentric distance along the LOS, r, which falls directly on the LOS (see left panel of Figure 2 for a single PBH example).

Each PBH then needs two additional dimensional quantities for a final three-dimensional position within the LOS cylinder. We project each PBH onto a circular cross section of the LOS cylinder at sampled distance r; then, assuming an isotropic projection distribution, we sample radial and angular component values for each PBH (see middle panel of Figure 2 for a single PBH example). For each PBH, radial distance (from the center axis of the LOS cylinder to the projected field radius, R) is sampled proportional to the cylindrical cross-sectional area ($\pi \hat{R}^2$), while an angle is uniformly sampled between [0, 2π].[11]

The result of this sampling process is a cylinder along the LOS populated with the number of PBHs determined by Equation (5), following that of the halo profile in Equation (4). We performed convergence checks on the discritized space and find that as one passes over the Galactic center, distances within $\approx$0.157 kpc of the center cause the density to converge, so for our simulations we do not go below this distance radially from the Galactic center. Before velocity assignment, we mask out PBHs that cannot be observed by cutting out PBHs which fall outside of the survey light cone (i.e., solid angle). An example of this cut is shown in the right panel of Figure 2.

3.4. PBH Velocities

Each PBH is assigned a mean speed $\langle v \rangle$ given its galactocentric radius, using the Eddington formalism

[10] This approximation becomes less accurate as R increases, however we expect this error to be subdominant to other approximations, as we simulate at most 0.34 deg^2.

[11] This cumulative integration technique neglects correlation between mass and dark matter halo location (as dynamical friction forces on an extended PBH mass spectrum might introduce).

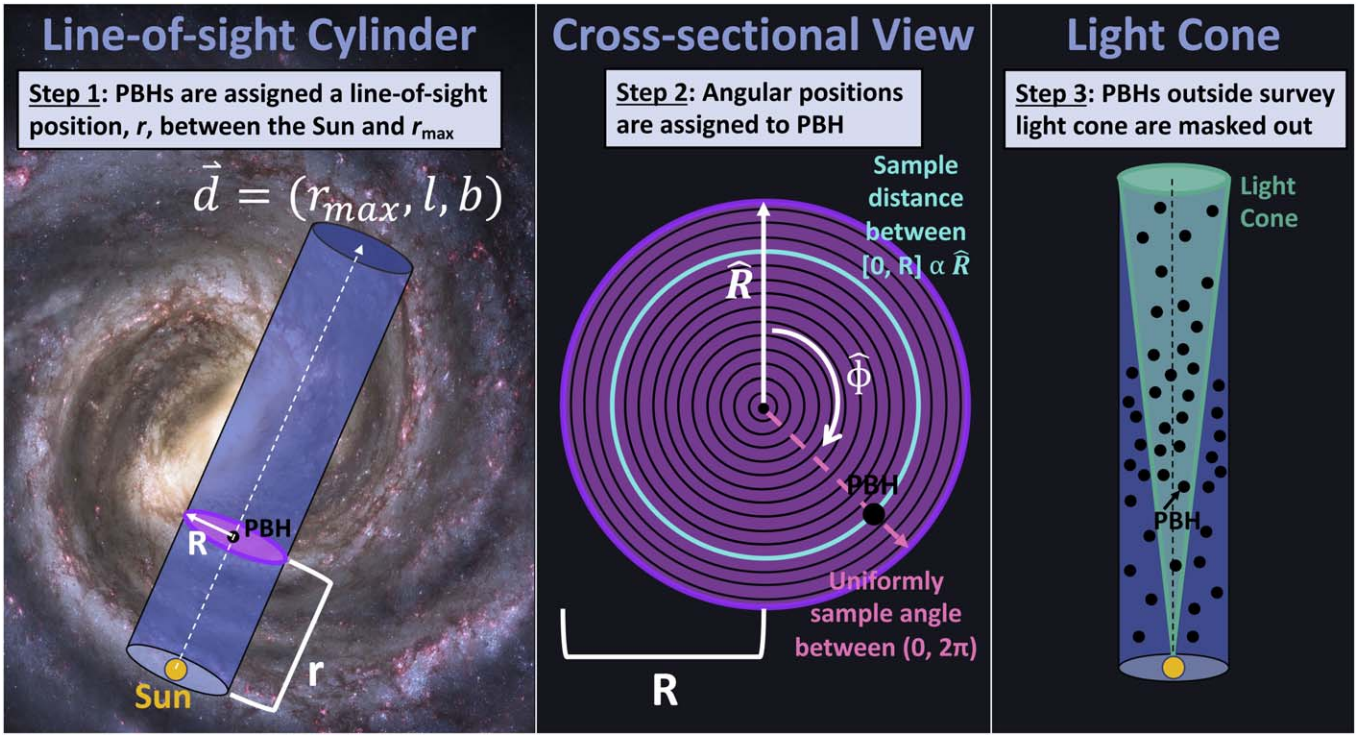

Figure 2. PBH position assignment for a single PBH in a simulation. Left: a cylinder is constructed with radius R (the survey radius projected at r_{max}) and centered on the LOS (dotted line extending from the Sun to the field center). PBHs are assigned a distance, r, between [0, r_{max}] by uniformly sampling the cumulative distribution function of Equation (4) using standard inverse transform sampling methods. Middle: a cross-sectional view of the LOS cylinder for the location assignment of a single PBH. Three-dimensional positions within the LOS cylinder are assigned by randomly sampling a radial distance $\hat{R}$ between [0, R] (proportional to the cross-sectional area, $\pi\hat{R}^2$) and uniformly sampling an angle between [0, 2π]. This is repeated until each PBH has a three-dimensional position within the cylinder. Right: PBHs that fall outside of the survey light cone are masked out.

(Eddington 1916) for the halo velocity as derived in Lacroix et al. (2018). The Eddington inversion model (which relates total gravitational potential and mass density to the dark matter phase-space distribution) deviates from the standard halo model (SHM; in which velocities follow a truncated Gaussian), especially at smaller galactic radii (see "SHM" curve on lower panel of Figure 1). However, Lacroix et al. (2018) think the Eddington model more representative of PBH velocities, thus we use the NFW parameterization of this relationship (illustrated by the $\gamma = 1$ panel on Figure 1).

Next, we assume a Maxwellian velocity distribution, and for each PBH we use its assigned $\langle v \rangle$ as the distribution mean to get the Maxwell distribution parameter:

$$a = \frac{1}{2}\langle v \rangle \sqrt{\frac{\pi}{2}},$$

then calculate the probability density function:

$$f(v) = \sqrt{\frac{2}{\pi}} \frac{v^2 e^{-\frac{v^2}{2a^2}}}{a^3}, \tag{6}$$

in which v is the rms velocity. We uniformly sample a single value from the cumulative distribution function (again using inverse transform sampling):

$$F(v) = \int f(v) = \mathrm{erf}\left(\frac{v}{a\sqrt{2}}\right) - \sqrt{\frac{2}{\pi}} \frac{v e^{\frac{-v^2}{2a^2}}}{a}, \tag{7}$$

where erf is the error function. Each PBH is assigned the corresponding sampled rms velocity.

We let v take values between zero and the escape velocity $v_{esc} = 550$ km s^{-1}, which is consistent with current estimates, such as those from the Radial Velocity Experiment survey (Smith et al. 2007; Piffl et al. 2014). For PBHs with $\langle v \rangle <$ 250 km s^{-1}, this v_{esc} cut filters out <1% of the PBH distribution, while PBHs with mean speeds closer to the maximum, $\langle v \rangle$ ~300 km s^{-1}, equates to a loss of ~3.5%. Because the number of PBHs in the LOS cylinder was previously selected to match the total mass of the cylinder, the number of PBH lensing events will be biased slightly low. Figure 3 illustrates $f(v)$ and $F(v)$ distribution examples (in the main figures and subfigures, respectively) for a few selected galactocentric PBH radii and γ values.

Following similar projection methods as described in Section 3.3, we take our velocity magnitude v, and randomly sample two angular components for latitudinal and longitudinal velocity components.[12] The longitudinal component is sampled uniformly between [0, 2π], while the latitudinal component is sampled uniformly on the unit sphere (i.e., uniform in cos(latitude) between [−1, 1]).

3.5. Other PBH Parameters

In addition to six-dimensional kinematics, `PopSyCLE` requires additional parameters for microlensing survey simulation. Because PBHs form in the early Universe and not through

[12] We assume a Maxwellian distribution for PBH velocities as a computational shortcut, but use mean speeds following the Eddington inversion results from Lacroix et al. (2018, which assumes velocities deviate from the truncated Maxwellian of the SHM). However, we do not expect this simplifying assumption to be a dominant source of uncertainty in our analysis.

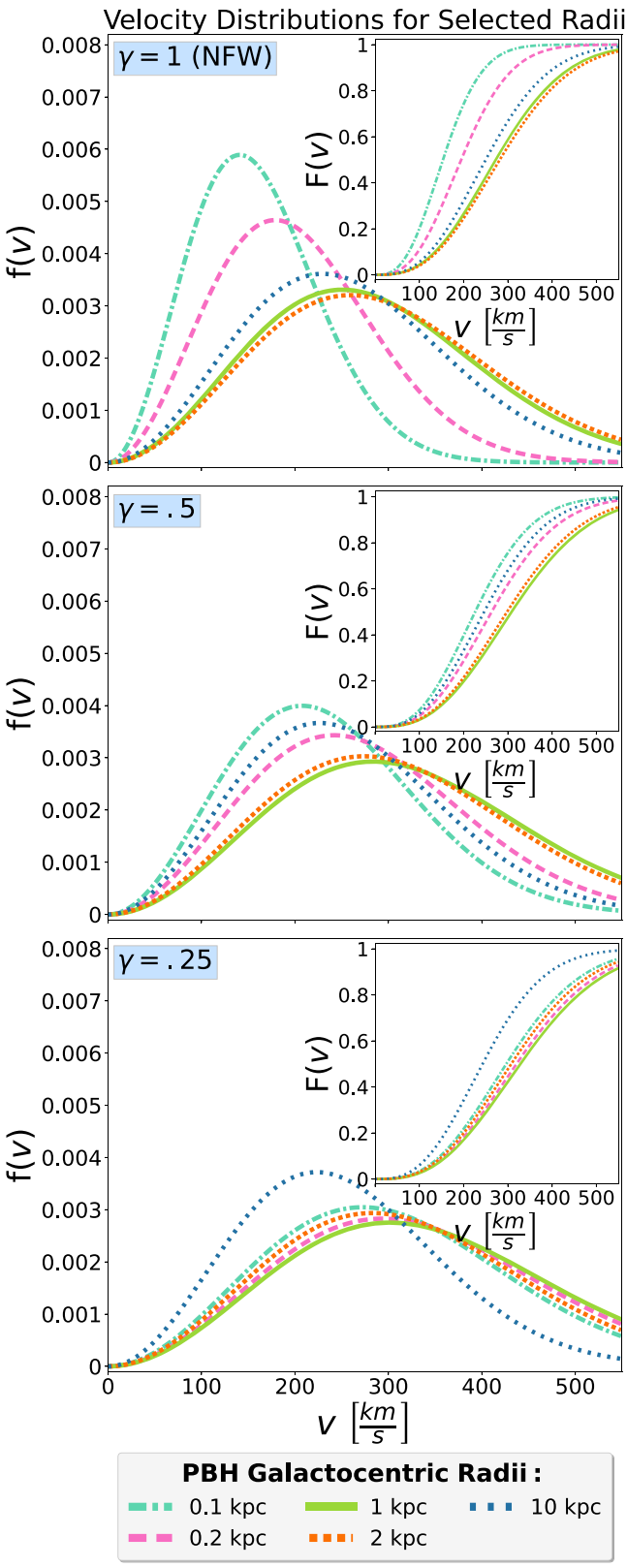

Figure 3. Velocity magnitude distributions for selected PBH radii, at three different γ values.

astrophysical formation channels, they do not have a ZAMS mass. However, to ensure smooth integration into PopSyCLE, the PBH mass at the time of the simulation is assigned as the ZAMS mass. We add a population type for PBHs, dubbed "dark matter halo" (in addition to those supplied by Galaxia), and assign an age of 13.8 Gyr. In addition to the PopSyCLE remnant IDs of 0 (star), 101 (WD), 102 (NS), and 103 (BH), a new remnant ID of 104 is assigned to PBHs. Magnitudes and photometric information do not need to be considered, as PBHs are "dark."

Table 2
PopSyCLE Survey Parameters

Parameter	Mock OGLE-IV		Mock Roman
	EWS Cut	Mróz19 Cut	
Duration	2920 days	2920 days	1825 days
Cadence[a]	∼2.5 days[b]	∼2.5 days[b]	∼3 days
$\theta_{\rm blend}$	0.″65	0.″65	0.″09
$u_{0,\rm max}$	$\leqslant$2	$\leqslant$1	$\leqslant$2
Area	0.34 deg^2	0.34 deg^2	0.16 deg^2
Min. mag.[c]	$\leqslant$21.0	$\leqslant$21.0	$\leqslant$26.7
Filter	I_V	I_V	H_{AB}
$\Delta_{\rm mag}$	$\geqslant$0.1	⋯	$\geqslant$0.1
t_E	⋯	$0.5 \leqslant t_E \leqslant 300$	⋯

Notes.
[a] PopSyCLE-defined cadence, which does not account for daytime gaps or survey gaps.
[b] Fields BLG-500 and BLG-611 use a PopSyCLE survey cadence of 10 days.
[c] Mock EWS and Mock Roman use minimum baseline magnitude. Mock Mróz19 uses minimum source magnitude.

4. Microlensing Simulations

Each of our mock surveys closely resemble the observational criteria for the survey being simulated. The PopSyCLE survey parameters used are listed in Table 2, and include duration (length of the survey), cadence (time between each observation), $\theta_{\rm blend}$ (seeing-disk radius) and $u_{0,\rm max}$ (maximum impact parameter) as described in Section 2.3, area (surface area of the survey field of view projected on the sky), limiting magnitude of the survey, optical filter for the survey, $\Delta_{\rm mag}$ ("bump magnitude"; the difference between baseline magnitude and peak magnitude, used to remove low-amplitude events), and t_e (the Einstein crossing time described in Section 1). For this work, we assume a NFW dark matter profile, and use $\gamma = 1$ when generating the PBH population. PopSyCLE and SPISEA use the Vega magnitude system (denoted by subscript V), which we convert to AB magnitudes (denoted by subscript AB) where appropriate using values from Table 1 of Blanton & Roweis (2007).

The PopSyCLE cadence and actual observational cadence do not exactly correlate, as PopSyCLE spreads out observations over the user-specified duration, and with the user-specified cadence, not necessarily accounting for daytime or seasonal gaps. Our Optical Gravitational Lensing Experiment (OGLE) cadences are derived from the reported observations per field each night, and Nancy Grace Roman Space Telescope (Roman) cadences are determined by spreading the expected microlensing survey over the duration of telescope operation, meaning we neglect these daytime and seasonal gaps as well (discussed further in Sections 4.1 and 4.2). This choice of cadence may lead to underestimating the number of events with timescales shorter than the specified cadence, but we find this effect negligible.

For each survey, we specify a set of fields to run PopSyCLE on. Fields and locations (with the area from Table 2 drawn to scale) are detailed in Figure 4. Each field in Figure 4 is run one time at minimum, where light pink denotes each simulated OGLE-IV field that is run only once, dark pink denotes each

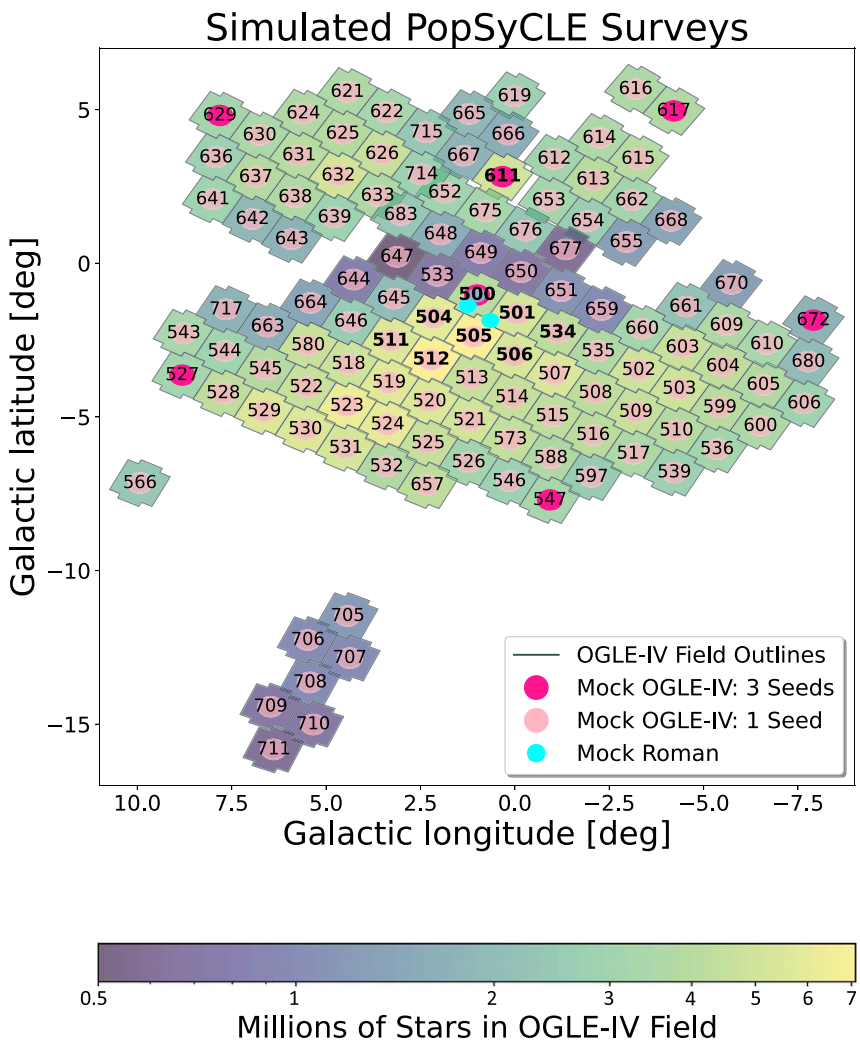

Field Name	Galactic Longitude	Galactic Latitude
BLG-500*	1.00°	-1.03°
BLG-527	8.81°	-3.64°
BLG-547	-0.93°	-7.70°
BLG-611	0.33°	2.82°
BLG-617	-4.21°	4.96°
BLG-629	7.81°	4.81°
BLG-672	-7.91°	-1.85°
MOA-II-gb5	0.65°	-1.86°
OGLE-2014-BLG-0613a†	1.25°	-1.38°

Figure 4. Left: simulated survey areas (drawn to scale) plotted over the OGLE-IV survey footprint. The background color scale represents the number of stars in a given field, and the number on each field is the OGLE bulge (BLG) field number. Each light pink field was simulated with one seed, while the dark pink fields were simulated with three seeds each. The fields that have their numbers in bold are the high-cadence OGLE-IV fields (as defined in Mróz et al. 2019), and everything else is considered a low-cadence field. Right: the name and Galactic coordinates for each field that was simulated three times (each field is centered on the given coordinates, and has a simulated area specified in Table 2). * BLG-500 is both a 0.34 deg^2 Mock OGLE-IV field and a 0.16 deg^2 Mock Roman field. † OGLE-2014-BLG-0613a is centered on a microlensing event reported by OGLE EWS.

OGLE-IV field that is run over three random seeds each, and cyan denotes each simulated Roman field that is run over three random seeds each. The dark pink and cyan fields are nine fields taken from Lam et al. (2020), in which each field is centered at a Galactic longitude and Galactic latitude (l and b, respectively, noted on the right panel of Figure 4) that either corresponds to the center of a bulge field from the OGLE survey (Udalski et al. 1992) or the Microlensing Observations in Astrophysics survey (Muraki et al. 1999). Only a 0.34 deg^2 or 0.16 deg^2 (for OGLE-IV and Roman, respectively) portion of each survey footprints is simulated, then extrapolation is done (when necessary) with the assumption that stellar density is constant over each field. Fields with a label in bold on Figure 4 are "high-cadence" OGLE-IV fields (as defined in Mróz et al. 2019), while everything else is considered a low-cadence field.

4.1. Mock OGLE-IV Simulations

The OGLE survey (Udalski et al. 1992) is designed to detect microlensing events in the Milky Way's bulge and Magellanic Clouds by frequently surveying the sky to look for microlensing signatures. OGLE phase 1 (OGLE-I) began in 1992, and recently finished the fourth phase (OGLE-IV), making observations with the 1.3 m Warsaw telescope at the Las Campanas Observatory in Chile over an 8 yr period (Udalski et al. 2015).

Our "Mock OGLE-IV" surveys use the corresponding values from Table 2 to simulate the portions of the OGLE microlensing survey shown in light pink and dark pink on Figure 4. We adopt these field parameters from the "Mock EWS" and "Mock Mróz19" surveys from Lam et al. (2020).[13] The Mróz19 cut returns OGLE-IV events that might be detectable, and that are also of sufficient signal-to-noise ratio (S/N) such that their lensing parameters could be reasonably estimated. The EWS cut includes additional events that could

[13] EWS = Early Warning System. The EWS reduces OGLE data in real time to alert on potential microlensing events. We base parameter estimates on reported numbers from 2016 to 2018.

conceivably be detected with OGLE, but that one may not be able to get reliable lensing parameter estimates for.

Using Table 6 from Mróz et al. (2019), we calculate the average cadence for each OGLE field we simulate, then, averaging over all fields, we decide on a simulated survey cadence of one observation every ∼2.5 days (with the exception of BLG-500 and BLG-611, which use a cadence of 10 days due to computational constraints). Cadence affects the sensitivity of shorter-scale events (in which t_E is less than the time between observations) because the event will fall entirely between observations. While our simulated cadences are longer than some of the actual OGLE-IV field cadences, Lam et al. (2020) show that a cadence of $\leqslant$10 days is sufficient to provide an accurate prediction of the t_E distribution peak.

All quantities reported from our PopSyCLE simulations are considered as corrected, as PopSyCLE does not account for events that fall between gaps, noisy observations, etc.

To calculate event parameters with and without PBHs, we first determine the number of detectable stars in each field, N_s, by cutting the full object catalog from Galaxia on the limiting magnitude of the survey ($I_V = 21$). To estimate the number of microlensing events (not including PBHs) in each field for each OGLE-IV cut, including relevant scaling and correcting for the actual survey efficiencies, we use the following equation:

$$N_{\rm ev} = N_{\rm ev}^{\rm sim}\left(\frac{1.4}{0.34}\right)\left(\frac{N_{\rm star}^{\rm M19}}{N_s^{\rm M19}}\right)\langle\epsilon\rangle, \tag{8}$$

where $N_{\rm ev}^{\rm sim}$ is the number of simulated microlensing events (excluding PBHs) output from PopSyCLE (after the cuts from Table 2 are applied), (1.4/0.34) scales our simulated number of microlensing events up to the full field area, $N_{\rm star}^{\rm M19}$ is the number of stars being monitored in that particular OGLE-IV field (values taken from Table 6 of Mróz et al. 2019), $N_s^{\rm M19}$ is the number of sources in a field that are brighter than $I_V = 21$ (with blends accounted for; values from Table 7 of Mróz et al. 2019), and $\langle\epsilon\rangle$ is the mean efficiency averaged over all of our simulated microlensing events in that field (i.e., all events in $N_{\rm ev}^{\rm sim}$). The quantity $(N_{stars}^{\rm M19}/N_s^{\rm M19})$ serves as a luminosity completeness correction factor.

Then, to estimate the number of PBH microlensing events in each field, with relevant survey and efficiency corrections included, for each OGLE-IV cut we use the following equation:

$$N_{\rm ev,\ PBH} = N_{\rm ev,\ PBH}^{\rm sim}\left(\frac{N_{\rm ev}^{\rm obs}}{N_{\rm ev}^{\rm sim}\langle\epsilon\rangle + N_{\rm ev,\ PBH}^{\rm sim}\langle\epsilon'\rangle}\right)\langle\epsilon'\rangle, \tag{9}$$

where $N_{\rm ev,\ PBH}^{\rm sim}$ is the number of simulated PBH microlensing events output from PopSyCLE (after the cuts from Table 2 are applied), $N_{\rm ev}^{\rm obs}$ is the number of detected events listed in Table 7 of Mróz et al. (2019) or the number of events reported between the 2011 and 2018 EWS seasons (depending on which cut we are determining $N_{\rm ev,PBH}$ for), $N_{\rm ev}^{\rm sim}$ is the number of simulated microlensing events (excluding PBHs) output from PopSyCLE (after the cuts from Table 2 are applied), $\langle\epsilon\rangle$ is the mean efficiency averaged over all of our simulated microlensing events (excluding PBHs) in that field (i.e., all events in $N_{\rm ev}^{\rm sim}$), and $\langle\epsilon'\rangle$ is the mean efficiency averaged over each of our simulated PBH microlensing events in that field (i.e., all events in $N_{\rm ev,\ PBH}^{\rm sim}$). $N_{\rm PBH}^{\rm sim}$ and $(N_{\rm ev}^{\rm sim} + N_{\rm ev,\ PBH}^{\rm sim})$ both have a dependence on field area and corrections due to luminosity completeness, meaning that both the area and luminosity correction ratios cancel out and do not need to be considered for these calculations.

Efficiencies are calculated using each event t_E, with the published t_E versus efficiency binned values from the OGLE-IV survey.[14] For simulated Mróz19 fields that do not have PBH events, $\langle\epsilon'\rangle$ is taken to be the average efficiency value across all other fields that do have PBHs, $\langle\epsilon'\rangle = 0.268$. For simulated Mróz19 fields that do not have any events (i.e., the number of NS, BH, WD, star, and PBH events are all zero), $\langle\epsilon\rangle$ is taken to be the average efficiency value across all other fields that have nonzero events, $\langle\epsilon\rangle = 0.172$.

EWS efficiencies are unknown, therefore we assume $\langle\epsilon\rangle = \langle\epsilon'\rangle$. However, when calculating the number of events (excluding PBHs) for our EWS simulations, we repeat the process of finding $\langle\epsilon\rangle$ using the reported OGLE-IV efficiency values, and fields that do not have any simulated events get assigned the average efficiency value across all other fields with nonzero events: 0.169.

The event rate, Γ (which excludes PBH events), is calculated by dividing the number of events without PBHs, $N_{\rm ev}$, by the number of stars that fall above the limiting magnitude for the given survey, N_s, and then dividing by the given survey duration. We report our simulated OGLE-IV results in Table 3, which compares values from our analysis, with relevant quantities (i.e., N_s and $N_{\rm ev}$) scaled up from 0.34 deg^2 to the full field area, 1.4 deg^2, for equivalent comparison to their observational counterparts. We list N_s, Γ, $N_{\rm ev}$, and $N_{\rm ev,PBH}$ for our mock Mróz19 and Mock EWS cuts, and list N_s, Γ, and $N_{\rm ev}$ observational results reported by Mróz et al. (2019) or the EWS website. N_s and Γ are completeness corrected values, while $N_{\rm ev}$ and $N_{\rm ev,PBH}$ are not, but are appropriately scaled by the various factors listed in Equations (8) and (9) to make noncompleteness corrected values to compare to their OGLE-IV observational counterparts. Three values are listed for fields that are run over three seeds each, and Poisson noise is assumed for all simulated values (this is because the exact noise profile is hard to characterize, and our sample of seeds follows Poisson uncertainty).

Table 3 assumes that 100% of dark matter consists of PBHs. Figure 5 further illustrates the breakdown of the number of predicted PBH events per field, as a function of $f_{\rm DM}$. The high-cadence OGLE-IV fields (from Mróz et al. 2019, labeled in bold on the left panel of Figure 4) are plotted in color on Figure 5, while each low-cadence field is plotted as a gray line. The right panels of Figure 5 show the cumulative number of PBH events over each field, giving the total number of estimated events per survey. In all panels the number of PBH events is determined using Equation (9). Because Equation (9) has a factor of $f_{\rm DM}$ in each instance of $N_{\rm ev,\ PBH}^{\rm sim}$, there is a nonlinear dependence on $f_{\rm DM}$ in $N_{\rm ev,PBH}$, making some lines on Figure 5 curved.

We combine results across all simulated OGLE-IV fields with the EWS cut and plot the resulting π_E, t_E distribution for all events (see left panel of Figure 6). We then compare the t_E distributions between PBHs and all populations except PBHs, and then compare the fractional contributions between compact

[14] https://www.astrouw.edu.pl/ogle/ogle4/microlensing_maps/eff/

Table 3
OGLE-IV Event Statistic Comparison

OGLE Field	N_s		Γ				N_{ev}				$N_{ev,PBH}$	
	Mróz19 (10^6)	M/E	Mróz19	M (10^{-6} star^{-1} yr^{-1})	EWS	E	Mróz19	M	EWS	E	M	E
BLG-500	6.78	4.71	23.9	23.5	110.9	134.42	164	111.52	752.0	646.23	7.01	20.83
…	…	…	…	23.59	…	134.77	…	112.04	…	648.33	3.56	21.89
…	…	…	…	26.16	…	130.46	…	123.97	…	626.27	2.43	14.84
BLG-501	13.31	12.24	24.1	33.0	89.9	123.6	317	253.3	1197.0	947.3	13.0	40.9
BLG-502	10.02	4.67	11.0	10.3	31.8	39.7	171	43.9	319.0	160.1	17.8	17.6
BLG-503	10.7	5.25	5.5	7.8	14.2	24.3	91	33.6	152.0	97.9	11.7	13.4
BLG-504	11.86	4.34	16.9	18.4	77.9	98.6	225	70.6	924.0	383.9	9.4	27.0
BLG-505	19.02	9.88	22.2	24.2	71.2	92.5	441	143.2	1354.0	550.1	9.5	37.1
BLG-506	12.85	5.36	16.5	20.7	57.0	88.3	247	81.7	732.0	357.5	9.5	20.1
BLG-507	11.22	5.27	12.3	15.4	33.3	59.3	216	67.1	374.0	259.3	17.0	14.2
BLG-508	9.53	5.0	6.8	10.4	22.9	33.4	119	45.4	218.0	145.1	9.4	14.4
BLG-509	9.82	4.72	4.6	6.1	13.3	20.6	79	23.8	131.0	79.0	11.0	7.8
BLG-510	7.67	3.47	3.6	3.0	6.6	10.2	38	7.8	51.0	27.9	6.4	4.1
BLG-511	13.45	5.11	13.5	16.8	56.1	64.0	204	64.0	755.0	244.2	4.5	23.1
BLG-512	17.48	8.34	14.0	18.0	53.0	63.9	280	108.4	926.0	384.9	9.9	25.2
BLG-513	13.71	7.87	8.5	14.6	26.8	54.0	213	78.1	368.0	287.5	8.7	14.1
BLG-514	10.27	5.44	6.2	10.2	18.9	41.8	108	45.9	194.0	179.9	9.8	8.0
BLG-515	8.1	4.32	5.7	8.1	19.6	24.8	80	38.3	159.0	115.1	1.7	10.7
BLG-516	7.61	3.76	4.6	7.0	7.6	15.0	48	17.8	58.0	41.0	0.0	1.5
BLG-517	5.96	3.18	2.6	4.5	0.3	11.3	12	9.6	2.0	23.1	2.1	0.2
BLG-518	12.34	4.72	7.3	11.1	25.2	36.1	160	38.9	311.0	126.7	4.4	12.6
BLG-519	12.93	6.3	9.3	10.5	29.3	36.1	223	51.4	379.0	177.3	11.3	21.1
BLG-520	11.63	5.94	5.6	9.1	20.3	32.1	124	54.5	236.0	187.7	13.8	9.2
BLG-521	9.18	4.95	4.5	9.2	12.2	26.4	69	40.9	112.0	127.0	0.0	7.8
BLG-522	8.62	4.24	7.4	7.8	19.4	21.7	108	40.5	167.0	107.8	10.4	12.9
BLG-523	10.4	4.84	6.0	7.0	16.5	21.1	99	26.6	172.0	76.3	10.0	9.8
BLG-524	9.66	4.49	6.0	6.5	7.9	20.2	75	17.0	76.0	50.7	9.4	4.9
BLG-525	7.84	4.04	3.2	4.3	6.5	15.4	36	16.4	51.0	55.1	7.9	5.6
BLG-526	5.25	3.34	2.3	5.1	4.4	13.5	20	34.0	23.0	88.8	3.2	1.7
BLG-527	6.36	2.85	5.5	2.89	5.3	8.30	48	10.63	34.0	33.64	8.44	1.42
…	…	…	…	2.89	…	9.58	…	10.63	…	38.76	16.70	5.40
…	…	…	…	3.06	…	9.55	…	11.29	…	38.76	8.03	1.24
BLG-528	7.39	2.99	5.5	4.1	5.7	11.2	50	12.8	42.0	33.1	0.0	0.6
BLG-529	7.79	3.2	5.6	4.7	3.6	11.9	39	7.0	28.0	15.3	1.9	1.8
BLG-530	7.37	3.24	8.5	2.4	4.9	9.9	54	3.5	36.0	14.2	10.6	2.7
BLG-531	6.85	3.05	5.1	3.0	4.8	9.5	34	6.4	33.0	20.9	6.9	5.0
BLG-532	6.02	2.82	2.7	2.6	2.0	6.9	23	8.2	12.0	24.7	4.8	1.4
BLG-533	1.02	0.21	7.1	0.0	0.0	0.0	1	0.0	0.0	0.0	0.0	0.0
BLG-534	9.06	4.51	17.2	19.8	72.3	101.1	176	93.2	655.0	481.0	3.6	19.3
BLG-535	7.57	3.58	15.2	14.4	43.7	67.1	189	46.0	331.0	217.5	9.4	9.0
BLG-536	5.21	2.47	3.8	1.9	0.8	4.8	15	0.7	4.0	1.7	2.1	0.6
BLG-539	4.52	2.37	4.0	2.8	0.4	6.1	13	8.3	2.0	18.4	3.9	0.4
BLG-543	4.76	1.62	5.9	2.9	7.1	10.8	36	5.0	34.0	18.9	9.3	2.8
BLG-544	5.66	2.87	6.1	5.2	6.0	15.0	40	11.7	34.0	33.2	0.0	1.9
BLG-545	6.47	3.05	6.1	6.4	14.1	17.6	57	14.8	91.0	40.1	7.7	8.0
BLG-546	4.25	2.47	3.4	3.8	0.5	7.7	12	7.5	2.0	14.6	0.0	0.2
BLG-547	3.67	2.07	1.3	1.99	0.3	5.46	3	2.57	1.0	7.80	0.88	0.19
…	…	…	…	2.23	…	6.21	…	2.89	…	8.86	1.07	0.14
…	…	…	…	1.74	…	4.47	…	2.25	…	6.38	0.00	0.18
BLG-566	3.03	1.28	0.9	2.4	0.0	4.0	2	5.0	0.0	7.8	0.3	0.0
BLG-573	7.16	3.83	3.7	8.1	4.9	19.5	33	14.5	35.0	35.3	4.9	3.5
BLG-580	8.47	3.19	8.0	9.2	29.2	31.9	116	22.6	247.0	76.7	7.2	9.6
BLG-588	5.39	3.19	2.7	6.5	3.9	12.4	23	13.6	21.0	27.9	3.6	2.4
BLG-597	4.28	2.57	4.0	2.2	3.7	7.4	27	5.3	16.0	17.5	2.9	1.9
BLG-599	7.8	3.69	3.9	4.5	3.8	11.3	41	14.6	30.0	34.5	5.0	2.4
BLG-600	5.29	2.5	2.9	3.5	2.3	6.0	18	9.0	12.0	14.5	1.4	0.8
BLG-603	10.02	5.24	10.6	11.1	29.8	36.6	167	50.2	299.0	168.8	5.8	19.5
BLG-604	9.8	4.42	7.0	6.4	12.4	20.3	100	19.7	122.0	65.6	7.0	9.1
BLG-605	6.13	2.6	3.9	1.8	4.2	8.1	29	3.9	26.0	15.8	12.8	3.8
BLG-606	4.48	2.32	3.8	1.8	0.2	3.8	11	2.8	1.0	6.2	1.6	0.1
BLG-609	6.77	3.05	8.4	7.9	21.6	36.6	81	17.9	146.0	92.5	5.2	6.4
BLG-610	5.78	2.86	6.2	5.9	9.3	19.6	38	12.3	54.0	42.3	0.0	1.9

Table 3
(Continued)

OGLE Field	N_s		Γ				N_{ev}				$N_{ev,PBH}$	
	Mróz19 (10^6)	M/E	Mróz19	M (10^{-6} star^{-1} yr^{-1})	EWS	E	Mróz19	M	EWS	E	M	E
BLG-611	6.93	5.14	16.2	18.79	68.0	75.07	158	154.64	471.0	624.8	8.34	23.25
…	…	…	…	18.70	…	81.09	…	153.82	…	674.72	5.69	17.88
…	…	…	…	16.88	…	78.52	…	139.01	…	653.92	7.27	20.63
BLG-612	7.34	4.14	10.1	14.3	21.0	56.5	87	30.2	154.0	117.9	4.1	5.2
BLG-613	7.99	3.96	12.4	15.1	24.8	68.0	119	40.4	198.0	181.3	11.4	11.1
BLG-614	6.32	3.33	5.5	10.4	13.3	31.7	43	23.5	84.0	72.2	3.0	5.4
BLG-615	8.09	3.7	6.8	13.5	19.0	40.8	74	31.0	154.0	94.1	4.8	5.6
BLG-616	5.08	2.75	3.4	3.7	0.2	11.4	12	5.5	1.0	14.5	1.5	0.1
BLG-617	6.32	3.08	5.2	6.20	10.6	16.75	43	18.79	67.0	50.63	5.45	6.64
…	…	…	…	3.68	…	13.90	…	11.17	…	42.02	2.47	7.20
…	…	…	…	5.19	…	14.57	…	15.75	…	44.05	3.43	3.64
BLG-619	4.47	2.57	3.3	6.8	0.0	19.6	3	1.9	0.0	5.2	0.7	0.0
BLG-621	5.15	2.24	6.8	5.1	8.3	11.0	44	11.5	43.0	22.9	8.4	4.1
BLG-622	4.76	2.43	3.6	5.3	6.7	15.7	25	13.0	32.0	35.4	3.6	3.1
BLG-624	6.02	2.54	4.3	3.0	6.3	8.7	31	6.7	38.0	21.0	2.9	4.0
BLG-625	6.47	2.6	5.5	5.1	7.9	15.4	46	11.6	51.0	30.7	10.6	5.3
BLG-626	8.32	4.3	8.3	9.2	15.9	32.9	92	31.1	132.0	112.8	7.3	4.2
BLG-629	4.56	2.09	3.4	2.71	0.4	7.65	11	4.71	2.0	12.75	3.9	0.37
…	…	…	…	2.96	…	7.15	…	5.14	…	11.93	0.00	0.19
…	…	…	…	2.96	…	7.15	…	5.14	…	11.93	1.85	0.24
BLG-630	5.11	2.21	4.4	5.4	7.4	11.2	30	11.9	38.0	25.5	8.4	5.4
BLG-631	7.09	2.99	7.1	6.9	8.7	20.3	61	16.2	62.0	47.6	8.9	3.5
BLG-632	9.59	5.43	9.0	10.2	22.8	33.1	128	45.8	219.0	155.7	5.6	10.2
BLG-633	6.3	2.78	13.1	12.2	23.3	55.5	106	27.4	147.0	119.9	4.8	6.1
BLG-636	4.26	2.26	5.1	5.5	0.5	11.9	14	8.1	2.0	16.5	0.9	0.1
BLG-637	5.84	2.56	5.2	7.4	8.6	19.5	40	14.9	50.0	41.4	1.6	2.0
BLG-638	7.96	3.66	6.9	10.1	11.1	32.2	64	22.4	88.0	73.9	5.1	3.7
BLG-639	5.08	1.89	10.4	8.2	19.5	34.8	70	13.4	99.0	54.2	3.2	3.7
BLG-641	5.33	3.05	4.9	9.6	4.5	25.8	31	22.7	24.0	60.0	2.4	1.2
BLG-642	3.22	1.37	8.7	4.1	8.7	15.8	36	5.0	28.0	19.6	0.0	1.3
BLG-643	2.11	1.53	5.7	4.7	8.5	16.1	17	8.4	18.0	29.8	0.0	0.7
BLG-644	1.02	0.34	0.0	0.0	0.0	0.0	0	0.0	0.0	0.0	0.0	0.0
BLG-645	3.33	0.66	13.6	5.4	32.1	13.9	63	3.4	107.0	9.4	0.0	5.6
BLG-646	5.09	0.62	8.3	8.3	19.8	19.9	57	4.6	101.0	9.5	0.0	0.0
BLG-647	0.68	0.21	0.0	0.0	0.0	2.4	0	0.0	0.0	0.1	0.0	0.0
BLG-648	2.86	1.74	18.3	8.0	42.3	45.5	67	12.1	121.0	67.7	6.9	4.5
BLG-649	0.93	0.18	0.0	0.0	0.0	0.0	0	0.0	0.0	0.0	0.0	0.0
BLG-650	0.91	0.18	0.0	0.0	0.0	0.0	0	0.0	0.0	0.0	0.0	0.0
BLG-651	1.56	0.77	0.0	8.0	0.0	20.8	0	1.1	0.0	2.9	0.0	0.0
BLG-652	6.55	3.62	14.2	16.2	22.3	84.5	100	33.9	146.0	177.9	7.3	5.0
BLG-653	5.37	4.56	20.1	20.1	39.9	109.4	127	64.1	214.0	362.3	4.7	5.0
BLG-654	4.92	2.35	16.7	15.4	48.8	84.9	110	27.8	240.0	159.4	5.6	9.0
BLG-655	2.13	0.25	9.5	0.0	0.0	2.1	3	0.0	0.0	0.1	0.0	0.0
BLG-657	4.43	2.38	2.6	1.9	0.7	7.1	6	3.4	3.0	11.0	0.9	0.5
BLG-659	1.05	0.73	0.0	8.5	0.0	21.1	0	0.9	0.0	1.6	0.0	0.0
BLG-660	4.63	2.07	23.7	12.2	35.4	50.6	94	15.7	164.0	72.4	10.6	10.6
BLG-661	4.22	2.78	15.2	7.6	25.6	44.6	80	14.7	108.0	88.9	0.0	5.5
BLG-662	6.16	1.79	12.2	12.1	20.0	56.0	87	12.8	123.0	66.2	10.4	7.7
BLG-663	2.15	1.35	3.7	6.9	2.3	23.3	4	6.6	5.0	22.4	0.0	0.0
BLG-664	1.85	0.64	5.7	1.6	4.3	8.8	6	1.1	8.0	3.1	2.1	0.7
BLG-665	2.72	1.34	1.2	5.8	0.4	16.9	1	1.2	1.0	3.3	0.1	0.0
BLG-666	2.04	1.9	9.8	7.6	0.0	34.6	3	2.1	0.0	12.3	0.3	0.0
BLG-667	2.41	1.72	11.3	11.4	15.8	43.8	27	17.8	38.0	61.7	2.4	1.3
BLG-668	1.93	0.48	8.8	4.3	5.2	10.8	15	1.4	10.0	3.7	0.0	0.0
BLG-670	1.65	1.5	10.7	4.5	10.9	14.8	19	3.8	18.0	21.5	0.0	1.2
BLG-672	2.45	2.88	5.6	5.36	8.6	17.14	17	12.03	21.0	34.56	3.05	1.43
…	…	…	…	4.11	…	20.2	…	9.22	…	40.68	3.77	1.06
…	…	…	…	5.36	…	18.6	…	12.03	…	37.44	3.05	2.49
BLG-675	5.64	5.5	26.5	22.2	53.2	118.5	160	91.9	300.0	491.8	9.3	9.8
BLG-676	4.58	4.27	3.9	21.7	0.0	136.9	1	5.9	0.0	38.3	0.1	0.0
BLG-677	0.96	0.84	0.0	5.5	0.0	15.9	0	0.3	0.0	1.1	0.0	0.0
BLG-680	3.57	2.0	5.0	3.3	0.8	11.9	8	1.8	3.0	9.5	1.2	0.3

Table 3
(Continued)

OGLE Field	N_s		Γ				N_{ev}				$N_{ev,PBH}$	
	Mróz19 (10^6)	M/E	Mróz19	M (10^{-6} star^{-1} yr^{-1})	EWS	E	Mróz19	M	EWS	E	M	E
BLG-683	4.28	3.51	26.2	16.0	1.6	74.2	21	7.6	7.0	37.7	1.2	0.3
BLG-705	1.1	0.65	0.0	0.0	0.0	0.0	0	0.0	0.0	0.0	0.0	0.0
BLG-706	0.94	0.54	3.4	0.0	0.0	0.0	1	0.0	0.0	0.0	1.0	0.0
BLG-707	0.81	0.5	0.0	0.0	0.0	1.0	0	0.0	0.0	0.5	0.0	0.0
BLG-708	0.84	0.42	0.0	1.2	0.0	1.2	0	0.5	0.0	0.5	0.0	0.0
BLG-709	0.61	0.0	0.0	0.0	0.0	0.0	0	0.0	0.0	0.0	0.0	0.0
BLG-710	0.59	0.0	2.6	0.0	0.0	0.0	1	0.0	0.0	0.0	0.0	0.0
BLG-711	0.48	0.0	0.0	0.0	0.0	0.0	0	0.0	0.0	0.0	0.0	0.0
BLG-714	5.84	2.84	11.0	11.9	7.4	57.2	54	14.8	43.0	74.8	5.3	1.6
BLG-715	3.42	1.61	10.2	6.1	14.9	30.1	36	8.0	51.0	31.1	8.0	3.5
BLG-717	2.06	0.77	3.9	2.7	1.0	8.6	6	1.6	2.0	3.5	1.7	0.1

Notes. Microlensing estimates for the following, all scaled to the full OGLE-IV field area of 1.4 deg^2: (1) Mróz19: observational results from Mróz et al. (2019), (2) M: our "Mróz19 Cut" simulation results, (3) EWS: Early Warning System events triggered between the 2011 and 2018 OGLE-IV seasons, and (4) E: our "EWS Cut" simulation results. N_s is the completeness corrected number of stars brighter than the magnitude limit of the survey ($I_V = 21$), Γ is the completeness corrected event rate (excluding PBH events), N_{ev} is the appropriately scaled number of events excluding PBHs (using Equation (8)), and $N_{ev,PBH}$ is the number of scaled simulated PBH microlensing events (using Equation (9)). Columns with three values were run over three seeds each, while only one seed is run for each remaining OGLE-IV estimates. Poisson uncertainty is assumed for all simulated values.

object populations. The top panel of Figure 7 shows our simulated EWS t_E results. The upper row shows the t_E distributions for all populations combined, all populations except PBHs, and PBHs alone, while the bottom row shows the relative contribution of each object type to the total number of microlensing events, as a function of t_E. The columns of each panel correspond to $f_{DM} = 0.01$, 0.1, and 1, respectively. Both Figures 6 and 7 include values from one seed run per field, and are generated before applying any of the scaling factors given in Equations (8) or (9) i.e., these are the total subset of events output from `PopSyCLE` with only the cuts listed in Table 2).

4.2. Mock Roman Simulations

The Nancy Grace Roman Space Telescope (abbreviated "Roman" and previously named WFIRST; Spergel et al. 2015), is a space-based telescope set to launch in 2027. During Roman's ∼5 yr operation, Roman will conduct a microlensing survey toward the Galactic bulge consisting of a seven-field mosaic, over six 72 days seasons (Penny et al. 2019; Johnson et al. 2020). During each microlensing survey season, images are estimated to be taken every ∼15 minutes from one of the seven fields in the "Cycle 7" configuration (see Figure 7 of Penny et al. 2019; Johnson et al. 2020), the survey footprint of which spans roughly the region between $l \approx (-0.5, 1.5)$ and $b \approx (-0.5, -2)$.

Our Mock Roman survey uses the corresponding values from Table 2 to simulate the Mock Roman labeled fields in Figure 4, which cover a subset of the projected Roman microlensing survey footprint. The values in this table match the "Mock WFIRST" values from Lam et al. (2020), which come from a combination of Penny et al. (2019) and OGLE EWS values, and are described by Lam et al. (2020) as "reasonable criteria expected for the mission." Each field is simulated three times, each with a different random seed, with all calculated quantities reported in this work using the average of all simulated results from that field. We assume constant stellar density over each simulated field whenever interpolating results.

The Roman microlensing survey will be divided up into seasons throughout Roman's operation (exact dates are not yet confirmed), with an expected operational timeline of ∼5 yr. Due to the microlensing survey seasons not being fully defined, we choose to spread the total microlensing survey over the estimated operational time, then scale observing frequency accordingly. Given the six planned seasons, each 72 days in length, with ∼96 observations each day, we estimate 41,472 observations total. Then, spreading the number of observations equally over the 5 yr estimated timeline works out to ∼23 observations per day. Because `PopSyCLE`'s cadence does not account for various time gaps, we evenly spread the observations over the telescope duration, ignoring daytime gaps and survey gaps. Because we do not expect any PBH events with $t_E < 10$ days, and we want to improve our computational feasibility, we choose to slow the cadence to one observation every 3 days. This enables us to stay within our computational boundaries, while still accurately representing the t_E distribution peak for all other compact objects.

Slowing the cadence this way can lead to underestimating the number of potentially detectable events, however our choice of cadence should not affect the BH and PBH populations. Additionally, the actual Roman survey layout (i.e., seasons throughout telescope operation) will lead to event overestimation, as some events will fall entirely within observing gaps between seasons, or will be missed by only detecting one side of the light curve, etc. The actual Roman survey may be more sensitive to short duration events, but fail to detect a fraction of events with timescales that fall between seasons (which can be >200 days if seasons are evenly spaced out over operation), which are detected in our `PopSyCLE` simulations. We estimate these gross cadence and duration approximations to be sufficient for an order-of-magnitude estimate of the number of PBH microlensing events expected with Roman.

The right panel of Figure 6 illustrates the π_E, t_E distribution for all events from all object populations, and the lower panel of Figure 7 shows the t_E distributions and fractional t_E contribution across populations for our Mock Roman

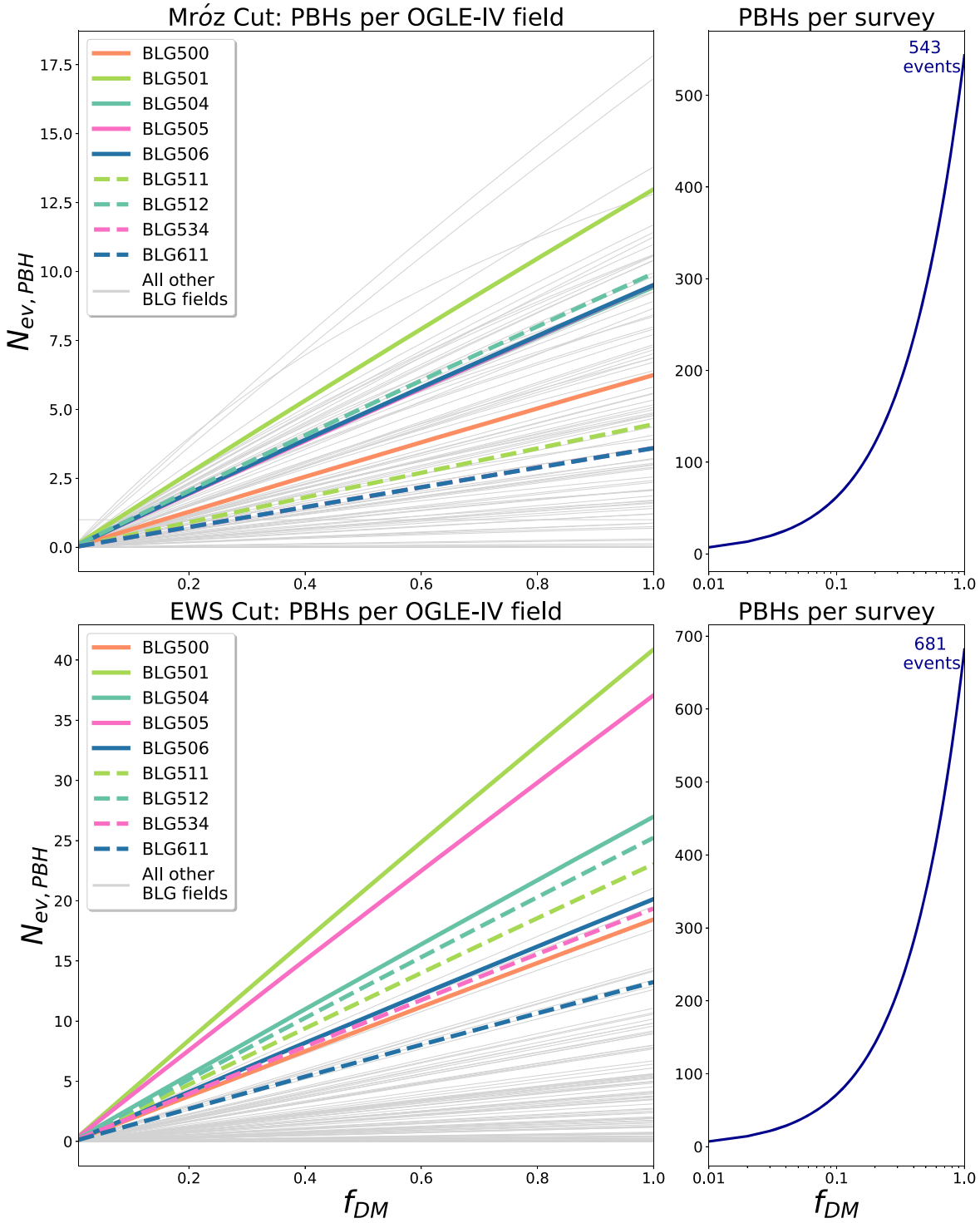

Figure 5. OGLE-IV PBH microlensing event ($N_{\rm ev,PBH}$) estimation as a function of dark matter fraction ($f_{\rm DM}$). Upper left: PBH event estimation per OGLE-IV field, for our Mock Mróz19 simulations. High-cadence and low-cadence OGLE-IV BLG fields are shown with bold colored lines, and thin gray lines, respectively. Upper right: cumulative PBH event estimate over all fields, with the $f_{\rm DM} = 1$ estimate reported. Lower left: same as upper left but for our EWS cut. Lower right: same as upper right but for our EWS cut. $N_{\rm ev,PBH}$ has a nonlinear dependence on $f_{\rm DM}$ (see Equation (9)), meaning lines on the left panel are not always linear.

simulations. Note that this plot reflects events from all three seed runs, from only a portion of the full Roman survey footprint, and has no scaling applied beyond the Table 2 cuts, as they are strictly for distribution demonstration.

Due to its resolving power and diffraction-limited seeing, Roman will be capable of obtaining simultaneous photometric and astrometric measurements from observed microlensing events, with an estimated astrometric precision (for isolated BHs) of ∼0.05 mas (Sanderson et al. 2019). Blending between the source and lens needs to be considered for luminous lenses, but this work primarily examines dark lenses, and thus we do not account for source–lens blending. We also choose to ignore blending from neighboring stars as we expect the scatter in including this blending to be subdominant to other simplifying assumptions. Therefore, we define the maximum astrometric shift as $\delta_{c,\rm max} = \delta_c$ (where δ_c is given in Equation (3)),

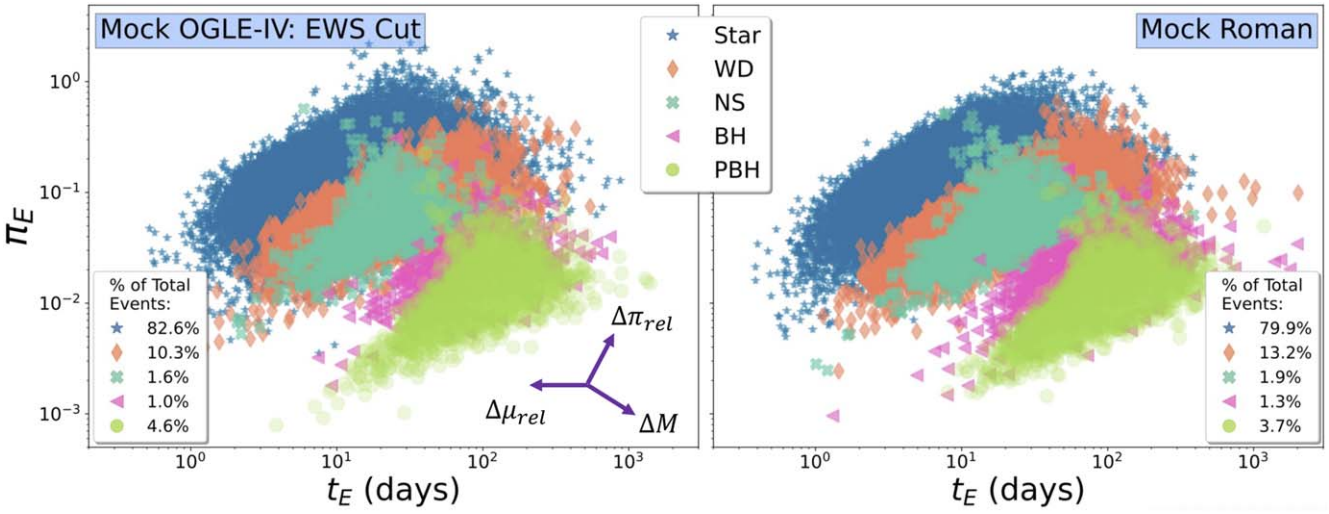

Figure 6. Simulated microlensing parallax (π_E) and Einstein crossing time (t_E) distributions. Left: Mock OGLE-IV simulation distribution after applying the Mock EWS observational cuts from Table 2. One seed run from each field is represented on this panel. Right: same as left panel, this time for Mock Roman. The arrows on the bottom of the left panel demonstrate the direction that points on this plot would shift, as a function of increasing the quantities specified. Only a small portion of the Roman survey footprint is simulated, and therefore only our simulated regions are represented within the right panel. This panel reflects events from all three seed runs per field. Neither panel considers any scaling or correction factors, and are considered the number of `PopSyCLE` detections given only the cuts from Table 2. This figure should be used for distribution demonstration purposes only.

calculated at the point in which the maximum astrometric shift occurs, $u = \pm\sqrt{2}$. This yields the maximum distance that the image will deviate from the expected path of the star with no lensing present. The left panel of Figure 8 illustrates $\delta_{c,\max}$ as a function of π_E, and includes a dashed line for the 3σ astrometric precision required for Roman ($\sim$0.15 mas) to detect isolated BHs.

Additionally, due to the assumed delta-function mass distribution for PBHs and NSs, they appear highly correlated in this space. However, extending the mass distributions will extend their footprint in this space, likely causing overlap with the BH population. Resulting $\delta_{c,\max}$ versus π_E distributions and $\delta_{c,\max}$ versus F146 AB source magnitude distributions for our Mock Roman simulation are shown on the left and right panels of Figure 8, respectively.

We estimate the number of PBH microlensing events that may be observed by Roman in three ways:

1. Less conservative cut: estimate the number of PBH events in each of our simulated 0.16 deg^2 fields by first averaging over the three seed runs per field, then scale the results up from 3×0.16 deg^2 to the full Roman survey area of 1.97 deg^2.
2. More conservative cut: multiply the result from method 1 by the survey duty cycle:

$$\text{duty cycle} = \frac{6 \text{ seasons} \times 72 \text{ days}}{5 \text{ yr} \times 365.24 \frac{\text{days}}{\text{year}}} = 0.24. \quad (10)$$

3. Realistic cut: count up the number of events that fall both above the solid 100 exposure precision line on Figure 8 and to the left of the dotted $F146 = 26$ limiting magnitude limit line, divide results by 3 (as each of the three seeds is represented on that plot), then scale up from 3×0.16 deg^2 to the full Roman survey area of 1.97 deg^2.

To determine our realistic event estimate cut given survey magnitude and astrometric shift constraints, we first apply the observational cuts from Table 2. For the initial magnitude cut we remove events where the baseline magnitude (i.e., combined flux from source, lens, and neighbors) is $H_{\rm AB} > 26.7$ (Sanderson et al. 2019).[15] We then use Equation (1) from Wilson et al. (2023) to convert $H_{\rm AB}$, $J_{\rm AB}$, and $K_{\rm AB}$ into the Roman F146 AB magnitudes. Then, we use a modified version of Equation (4) from Fardeen et al. (2024) to estimate the astrometric detection threshold of Roman as a function of magnitude, given a single exposure:

$$\sigma_{\rm ast} = \text{MAX}(0.3,\ 10^{0.2 \times F146 - 4.23}). \quad (11)$$

Fardeen et al. (2024) uses a minimum astrometric precision of 0.1 mas, however that is the optimal Roman detection case. Our modified equation uses 0.3 mas as the minimum astrometric precision, which is the minimum value for Roman to "properly sample astrometry" at the saturation limit of $H_V \approx 18$ (Lam et al. 2023).

For the 100 exposure limit curve (the solid black line on the right panel of Figure 8), we assume $\sigma_{\rm ast} \propto 1/\sqrt{100}$. We note that this S/N calculation neglects the negative effect that blending will have on astrometric precision, as it leads to higher correlated noise and generally smaller astrometric signals, and is therefore overly optimistic when estimating the predicted number of astrometric events.[16]

The right panel of Figure 8 shows maximum astrometric shift, $\delta_{c,\max}$, versus F146 AB source magnitude, for each of our individual microlensing events. Also marked on this figure is Roman's estimated limiting magnitude, F146 $\approx$26. Roman should be able to detect events that lie above the solid black line, and that fall below the limiting magnitude of the survey (which we estimate here as falling to the left of the dashed line at F146 = 26). Figure 8 includes the full distribution of events over all three seeds, over all three simulated Roman fields, and assume not scaling ratios or cuts other than those from Table 2.

[15] $H_{\rm AB} =$ 26.7 is the Roman High-Latitude Survey limit for faint point sources (Sanderson et al. 2019). We assume this value to be an appropriate initial cut.

[16] For Roman, when the magnitude $F146 < 26$, the density of sources is expected to be $\approx$10 stars per arcsecond (Penny et al. 2019), which will make precision astrometry challenging.

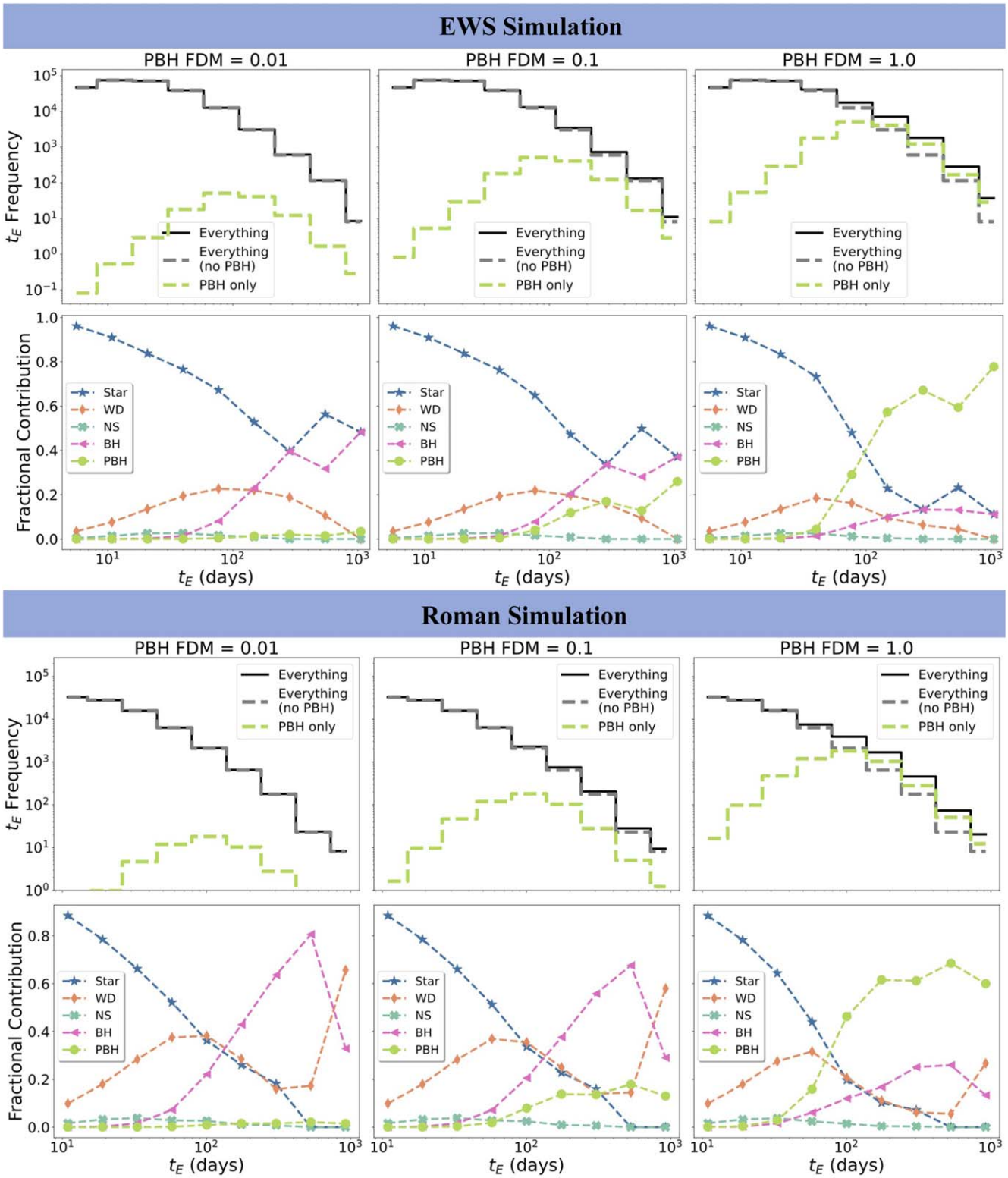

Figure 7. t_E distributions and fractional contributions across various compact object populations. Upper: Mock OGLE-IV simulations (EWS cut) results, from one seed per field. Lower: Mock Roman survey results, including all three seed runs for each of the three simulated Roman fields. The left, middle, and right columns of each panel correspond to $f_{\rm DM} = 1$, $f_{\rm DM} = 0.1$, and $f_{\rm DM} = 0.01$, respectively. The upper row of each panel has three t_E distributions: all compact object populations, all populations except PBHs, and only the PBH population. Median PBH t_E values are shown by the dotted vertical lines. The lower row of each panel shows the fractional t_E contribution from each population as a function of Einstein crossing time. This figure should be used for distribution demonstration purposes only.

5. Results

Adding a PBH model to `PopSyCLE` serves as a capable means for simulating PBH dark matter, enabling us to estimate the number and statistical distribution of detectable PBH microlensing events for various microlensing surveys and to constrain the abundance of PBH dark matter in the Milky Way. Throughout the remainder of this section we discuss the results

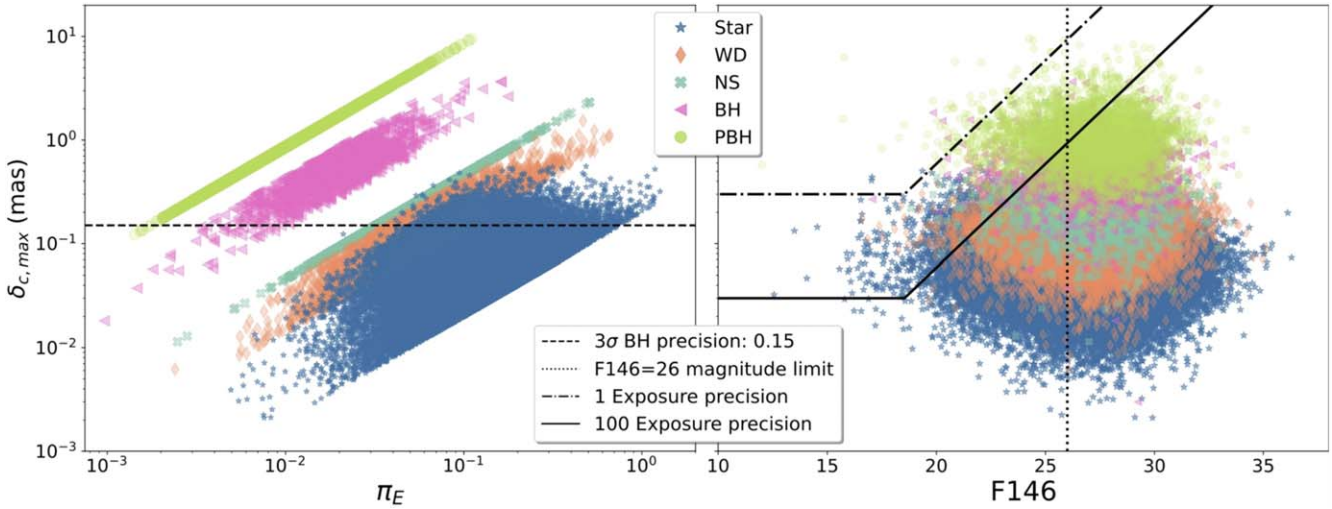

Figure 8. Simulated Roman survey distributions, after cuts from Table 2. Left: maximum astrometric shift ($\delta_{c,\max}$) versus microlensing parallax (π_E). Right: maximum astrometric shift ($\delta_{c,\max}$) versus F146 AB source magnitude. The horizontal dashed line represents the 3σ astrometric precision required for Roman ($\sim$0.15 mas) to detect isolated BHs (Sanderson et al. 2019), the vertical dotted line represents the approximate limiting magnitude for Roman (F146 $\approx$26), and the two diagonal lines represent the one exposure (dashed–dotted line) and 100 exposure (solid line) estimated precision curves. Roman should be able to detect events that fall above the solid black line and that fall below (i.e., to the left of) the limiting magnitude of the survey. Note that this plot includes events from simulations on only a small portion of the full planned survey footprint, all three seed runs per simulated field are included in this figure, and events represented here include only the cuts from Table 2.

from our Mock OGLE-IV and Mock Roman simulations, comparing estimated photometric and astrometric measurement distributions between PBHs and other compact object populations, using similar analysis techniques as used by Lam et al. (2020).

Lam et al. (2020) find that analyzing microlensing events in π_E, t_E space proves to be a compelling way of disentangling BHs from other types of lenses, given only photometric information. While π_E, t_E space can enable ensemble statistical constraints, it does have real-time alert limitations. Lam et al. (2020) notes that this analysis cannot serve as criteria for astrometric follow-up selection, as π_E is difficult to measure precisely at or before the time of the photometric peak of the light curve occurs. Fortunately, the next wave of microlensing surveys (e.g., Roman) are expected to obtain simultaneous photometric and astrometric observations, and Lam et al. (2020) further finds that combining photometric analysis with astrometric measurements has the ability to further increase separability between populations, making `PopSyCLE` a powerful tool for potentially differentiating PBHs from other compact objects in these parameter spaces.

5.1. Mock OGLE-IV

Given the resulting PBH event distributions from Figure 6, we find that 30 $M_\odot$ PBH events tend toward higher t_E and lower π_E, but that the population significantly overlaps the stellar evolved BH distribution. This overlap is likely due to our choice of PBH mass, as we would only expect PBHs to shift in this space by a factor of $1/\sqrt{\bar{m}_{\rm BH}}$ in π_E, and by a factor of $\sqrt{\bar{m}_{\rm BH}}$ in t_E. Additionally, the median $\mu_{\rm rel}$ is slightly higher for PBHs than BHs, with $\mu_{\rm rel,PBH}$ $\sim$12.5 and $\mu_{\rm rel,BH}$ $\sim$7.1 (averaged between the Mróz19 and EWS cuts), causing an additional shift to lower t_E, undoing some of the offset shift to higher t_E due to the higher PBH masses.

Comparing the t_E distributions with and without PBHs in Figure 7 reveals that PBH microlensing events peak at longer duration t_E than other compact objects, with a peak of $\sim$91.7 days for both our Mróz19 and EWS cuts. Additionally, analyzing the fractional contribution of PBH to BH events in our EWS cut simulations (using the full distribution of events after only the cuts from Table 2), we find $\sim 4.3 f_{\rm DM}$ times more PBH events than BH events. Note that our results use a higher cadence than the Lam et al. (2020) "v3" results, catching more events with long duration. However, when running our simulations without PBHs using the exact same simulation parameters as Lam et al. (2020), we find identical results to those reported in Lam et al. (2020, Appendix A.1) and by Rose et al. (2022).

We find a small shift in Einstein crossing time peak values between our simulations and Mróz et al. (2019; consistant with Rose et al. 2022), likely due to field-of-view extrapolation and the absence of binary lenses and binary sources, which should not have a significant impact on our predicted long-duration PBH events. Similar to Rose et al. (2022) and Lam et al. (2020), our star counts and event rates can be off from Mróz et al. (2019) and EWS estimates by a factor of $\approx$2 (see Table 3). The star count differences are not due to stellar binarity or confusion (N. Abrams et al. 2024, in preparation, Rose et al. 2022), and the event-rate discrepancies may be due to the galactic model chosen for our simulations and extinction being variable closer to the Galactic bulge (Lam et al. 2020). It is worth noting that our EWS-predicted PBH event rates will be artificially low, as we have not accounted for spurious and anomalous events, beyond our general scaling factor between our simulated results without PBHs versus the observational EWS results.

Given the results in Table 3 and Figure 5, we find that 681 PBH events may be within the 8 yr OGLE-IV data set, in which each PBH may conceivably be detected, but for which reliable lensing parameter estimates may not be attainable (i.e., EWS cuts). We additionally estimate 543 PBH events may be detectable and also have sufficient S/N such that lensing estimates can be reasonably estimated (i.e., Mróz19 cuts).

5.2. Mock Roman

Figure 6 illustrates the distribution results that we expect to be detectable in the upcoming Roman microlensing survey. We find a significant overlap between the PBH and BH populations that we expect to be for the same reason as described in Section 5.1, which is mainly due to our choice of $\bar{m}_{\rm PBH}$ and the resulting $\mu_{\rm rel}$ distributions, with median values of $\mu_{\rm rel,PBH}$ $\sim$11.3 and $\mu_{\rm rel,BH}$ $\sim$7.0. We find $\sim$2.8 $f_{\rm DM}$ times more PBH microlensing events than we do BH microlensing events, and find a peak t_E of $\sim$91.3 days. The estimated number of PBH events to BH events is lower than that of our simulated OGLE survey, but that is expected, as PBH events tend toward longer timescale events, and OGLE is a longer survey.

Given our simplified PBH model and assumed Roman microlensing survey structure, we estimate the number of potentially detectable PBH microlensing events expected with Roman using the three calculation methods outlined in Section 4.2. For scaling up from our simulated survey area of 0.48 deg^2 to the full Roman survey area of 1.97 deg^2, we account for the overlap between two of our simulated fields (where the overlap fraction = 0.19%). We assume constant stellar density over the Roman microlensing survey footprint, $\bar{m}_{\rm PBH} = 30\ M_\odot$, and that there are no survey gaps. For our less conservative event estimate (scaling method 1, that scales our predicted event rate up to the full survey area of 1.97 deg^2), we estimate 4981 events to be detectable with Roman. Our more conservative estimate (scaling method 2, which multiplies the result of scaling method 1 by the Roman duty cycle given in Equation (10), and then scales that result up to the full survey area of 1.97 deg^2) results in 1195 PBH events that might be detectable by the future Roman survey. Lastly, our realistic cut estimate (scaling method 3, which includes only the events that would fall above the solid 100 exposure precision line, and to the left of the limiting magnitude dashed line on Figure 8, and scaled to the full survey size) results in 1212 PBH events detectable by Roman.

Ignoring potentially important survey selection effects, the actual number of expected PBH lensing events will scale roughly proportionally to $f_{\rm DM}$ and approximately constant as a function of mass. Because we slow the cadence from $\sim$23 observations a day to one observation every 3 days (see calculations in Section 4.2), we underestimate the S/N of microlensing events by a factor of $\sim$8, and ultimately underestimate the number of microlensing events that may be detectable. However, we then overestimate the predicted number due to our survey gap assumptions, and assumption of a source-dominated noise regime. For these reasons, we expect our event estimates to conservatively hold to $\sim 1000 f_{\rm DM}$.

Analyzing event distributions in $\delta_{c,\rm max}$, π_E space (left panel of Figure 8) finds separability between the PBH and BH populations, more so than in π_E, t_E space. Note that because we use a delta-function PBH mass distribution, the astrometric shift appears as a perfect linear function in this space; however, exploring broader mass spectra will cause scatter about $\delta_{c,\rm max}$, likely causing overlap with the BH population. We then explore the compact object event distributions in three-dimensional π_E, t_E, $\mu_{\rm rel}$ space, and find complete separability between the PBH and BH populations (Figure 9). Again, this complete separability is likely due to our choice of a constant mass, however more analysis is needed to confirm how much overlap would appear in this space given an extended PBH mass distribution.

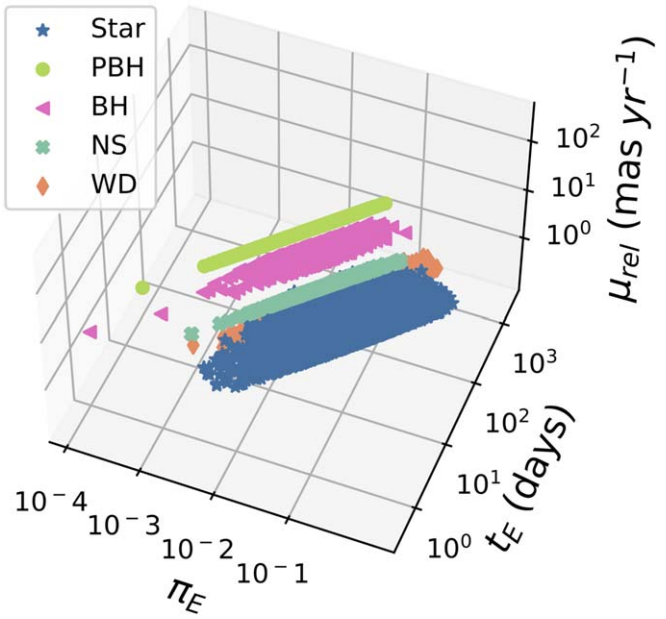

Figure 9. π_E, t_E, $\mu_{\rm rel}$ distribution of compact objects for our simulated Roman survey (using all three seeds from each of the three simulated fields, including only the cuts from Table 2). This figure demonstrates that while there is significant overlap of the BH and PBH populations in π_E, t_E space (Figure 6), there is potential to disentangle the populations with the addition of a $\mu_{\rm rel}$ component.

In general, decreasing $\bar{m}_{\rm PBH}$ will result in PBH microlensing events overlapping in π_E, t_E space with compact object microlensing events with similar masses, although different spatial and velocity distributions will not make this exact. Additionally, our simulations assume no blending, however, due to the sensitivity of Roman, binary sources and flux from neighboring background stars will dilute the astrometric signal, causing Figures 8 and 9 to change, introducing scatter in the $\delta_{c,\rm max}$ and $\mu_{\rm rel}$ dimensions. Penny et al. (2019) finds that the mean blend fraction of detected microlensing events is $\sim$0.2 meaning that the astrometric lensing signal could be diluted by a factor of $\sim$5. Regardless, our results demonstrates that accurate $\delta_{c,\rm max}$ and $\mu_{\rm rel}$ estimates will play an important role in separating PBH and BH events, making precise astrometric measurements with Roman a priority in the next decade of microlensing.

6. Discussion and Conclusion

Dark matter makes up $\sim$85% of the matter content in the Universe, and though not well understood may be predominately comprised of PBHs. Recent explorations have placed very tight constraints on $f_{\rm DM}$ covering many decades in mass (see summary in Bird et al. 2023). Due to cosmological constraints, stellar evolved BHs can only account for a small portion of dark matter (Collaboration et al. 2014), making detection and characterization of PBHs an important key in understanding the structure and formation of our Universe.

Throughout this work we have detailed and demonstrated the utility of adding a PBH population model into the microlensing simulation code `PopSyCLE`, enabling us to simulate microlensing surveys in the Milky Way, serving as a powerful tool for analyzing the estimated astrometric and photometric measurements of potential PBH microlensing events. Because this work is first and foremost a proof of concept for the

addition of PBHs to PopSyCLE simulations, we make many simplifying assumptions about PBHs (see Section 3) and microlensing survey parameters (see Section 4). We acknowledge our assumptions of $f_{\rm DM} = 1$ and a monochromatic PBH mass of $\bar{m}_{\rm PBH} = 30\ M_{\odot}$ do not necessarily align with recent constraints on $f_{\rm DM}$ (e.g., Alcock et al. 2001; Tisserand et al. 2007; Wyrzykowski et al. 2011; Blaineau et al. 2022) or the expectation of an extended mass distribution, however they enable us to demonstrate our PopSyCLE + PBH simulations, and allows the reader to scale our results to other values of $f_{\rm DM}$ and $\bar{m}_{\rm PBH}$ as they see fit. Reported results scale roughly proportional to $f_{\rm DM}$ and approximately constant as a function of mass, modulo potentially important survey selection effects.

Given our simplified PBH model and survey assumptions, we find the following:

1. Assuming a monochromatic PBH mass of $\bar{m}_{\rm PBH} = 30\ M_{\odot}$, PBH microlensing events tend toward longer duration (t_E), smaller parallax (π_E), larger maximum astrometric shift ($\delta_{c,\rm max}$), and larger source–lens proper motion ($\mu_{\rm rel}$) than BHs, but in most cases PBHs overlap with the stellar BH population.
2. We predict Roman will have the ability to detect $\sim 4981 f_{\rm DM}$ (scaling method 1, less conservative estimate, determined by area scaling ratios alone) PBH events, $\sim 1195 f_{\rm DM}$ (scaling method 2, more conservative estimate, determined by area scaling ratios between our simulations and the Roman survey, along with the Roman duty cycle of 0.24), and a more realistic estimate of $\sim 1212 f_{\rm DM}$ events (scaling method 3, considering events that would fall above the 100 exposure precision threshold for F146 source magnitude, and fall below the limiting magnitude of the survey, then scaling to the full survey area). These reported values assume that there is constant stellar density across Roman fields (allowing us to scale up to the full Roman survey area of 1.97 deg^2), no survey gaps, that $\bar{m}_{\rm PBH} = 30\ M_{\odot}$ lies within a mass range detectable by Roman with moderate efficiency, and that noise is in the source-dominated regime and neglects effects of blending. We expect this to hold to the order of $\sim 1000 f_{\rm DM}$ after taking into account the multiple overestimations and underestimations described throughout this work, which are due to PBH population and survey assumptions.
3. We find that ∼355 PBH events may be within the 8 yr OGLE-IV data set, in which each PBH may conceivably be detected, but for which reliable lensing parameter estimates may not be attainable. We additionally estimate ∼306 PBH events may be detectable and also have sufficient S/N such that lensing estimates can be reasonably estimated for each PBH. We expect this to hold on the order of $10^2 f_{\rm DM}$.
4. With the assumption of $\bar{m}_{\rm PBH} = 30$, we find $\sim 4.3 f_{\rm DM}$ and $\sim 2.8 f_{\rm DM}$ times more PBH microlensing events than BH microlensing events for our Mock OGLE-IV (EWS cut) and Roman simulations, respectively. The fraction of events is higher for the OGLE survey as it has a longer survey duration, and PBH microlensing events tend toward longer timescales. This averages out to $3.6 f_{\rm DM}$ more PBHs than BHs.
5. Using simulated PBH distributions with $f_{\rm DM} = 1$ and $\bar{m}_{\rm PBH} = 30$, we find median t_E values for our OGLE-IV EWS cut and Roman simulations of ∼91.7 days and ∼91.3 days, respectively, where peak t_E scales approximately proportional to $\sqrt{\bar{m}_{\rm PBH}}$. This results in an average PBH estimated peak Einstein crossing time of ∼91.5 days.

Roman will have the ability to conduct simultaneous photometric and astrometric observations, with an astrometric sensitivity that enables significant astrometric lensing measurement for the majority of events where $M_{\rm PBH} \geqslant 1\ M_{\odot}$ (see Figure 8). Therefore, we expect Roman to be an important instrument in the next decade of microlensing science (and for potential PBH detection), in that it will enable better disambiguation between the PBH and BH event populations in the π_E, t_E, $\delta_{c,\rm max}$, and $\mu_{\rm rel}$ parameter spaces. Due to the overlap between PBHs and BHs in these various spaces, and our average result of $\sim 3.6 f_{\rm DM}$ times more 30 $M_{\odot}$ PBH microlensing events than BH events, surveying the Magellanic Clouds may provide improved PBH dark matter fraction constraints, as the lower stellar density should result in a higher relative number of PBHs to BHs, enabling us to better constrain photometric and astrometric PBH parameters. To be able to simulate this, a Magellanic Cloud model would need to be added to PopSyCLE.

With all simplifying assumptions aside, we have demonstrated and validated our addition of a PBH model into PopSyCLE that can be used to analyze astrometric and photometric microlensing measurement predictions for PBHs, serving as a powerful tool in the next decade of microlensing science and astronomical surveys.

Acknowledgments

This work was performed under the auspices of the U.S. Department of Energy by Lawrence Livermore National Laboratory under Contract DE-AC52-07NA27344 and was supported by the LLNL-LDRD Program under Project Numbers 17-ERD-120 and 22-ERD-037, and by LLNL HEP Program Development. M.S.M acknowledges support from the University of California Office of the President for the UC Laboratory Fees Research Program In-Residence Graduate Fellowship (grant ID: LGF-19-600357). C.Y.L. and J.R.L. acknowledge support by the National Science Foundation under grant No. 1909641, the National Aeronautics and Space Administration (NASA) under contract No. NNG16PJ26C issued through the WFIRST (now Roman) Science Investigation Teams Program, and the Heising-Simons Foundation under grant No. 2022-3542. C.Y.L. also acknowledges support from NASA FINESST grant No. 80NSSC21K2043. LLNL-JRNL-834877.

ORCID iDs

Kerianne Pruett https://orcid.org/0000-0002-2911-8657
William Dawson https://orcid.org/0000-0003-0248-6123
Michael S. Medford https://orcid.org/0000-0002-7226-0659
Jessica R. Lu https://orcid.org/0000-0001-9611-0009
Casey Lam https://orcid.org/0000-0002-6406-1924
Scott Perkins https://orcid.org/0000-0002-5910-3114
Peter McGill https://orcid.org/0000-0002-1052-6749
Nathan Golovich https://orcid.org/0000-0003-2632-572X

References

Abbott, B. P., Abbott, R., Abbott, T. D., et al. 2016, PhRvL, 116, 061102
Abbott, B. P., Abbott, R., Abbott, T. D., et al. 2017a, PhRvL, 118, 221101
Abbott, B. P., Abbott, R., Abbott, T. D., et al. 2017b, PhRvL, 119, 141101
Alcock, C., Akerlof, C. W., Allsman, R. A., et al. 1993, Natur, 365, 621

Alcock, C., Allsman, R. A., Alves, D. R., et al. 2001, ApJL, 550, L169
Aubourg, E., Bareyre, P., Bréhin, S., et al. 1993, Natur, 365, 623
Bird, S., Albert, A., Dawson, W., et al. 2023, PDU, 41, 101231
Bird, S., Cholis, I., Muñoz, J. B., et al. 2016, PhRvL, 116, 201301
Blaineau, T., Moniez, M., Afonso, C., et al. 2022, A&A, 664, A106
Blanton, M. R., & Roweis, S. 2007, AJ, 133, 734
Carr, B., & Kuhnel, F. 2021, arXiv:2110.02821
Carr, B., & Silk, J. 2018, MNRAS, 478, 3756
Carr, B. J. 1975, ApJ, 201, 1
Chapline, G., & Barbieri, J. 2018, LHEP, 1, 17
Chapline, G. F. 1975a, PhRvD, 12, 2949
Chapline, G. F. 1975b, Natur, 253, 251
Chapline, G. F., & Frampton, P. H. 2016, JCAP, 2016, 042
Chatzopoulos, S., Fritz, T. K., Gerhard, O., et al. 2015, MNRAS, 447, 948
Collaboration, P., Ade, P. A. R., Aghanim, N., et al. 2014, A&A, 571, A16
Croon, D., McKeen, D., Raj, N., & Wang, Z. 2020, PhRvD, 102, 083021
Damineli, A., Almeida, L. A., Blum, R. D., et al. 2016, MNRAS, 463, 2653
Eddington, A. S. 1916, MNRAS, 76, 572
Fardeen, J., McGill, P., Perkins, S. E., et al. 2024, ApJ, 965, 138
Gillessen, S., Eisenhauer, F., Trippe, S., et al. 2009, ApJ, 692, 1075
Hawking, S. 1971, MNRAS, 152, 75
Hawking, S. W. 1974, Natur, 248, 30
Hosek, M. W., Jr, Lu, J. R., Lam, C. Y., et al. 2020, AJ, 160, 143
Johnson, S. A., Penny, M., Gaudi, B. S., et al. 2020, AJ, 160, 123
Lacroix, T., Stref, M., & Lavalle, J. 2018, JCAP, 2018, 040
Lam, C. Y., Abrams, N., Andrews, J., et al. 2023, arXiv:2306.12514
Lam, C. Y., Lu, J. R., Hosek, M. W., Dawson, W. A., & Golovich, N. R. 2020, ApJ, 889, 31
Lu, J. R., Lam, C. Y., Medford, M., Dawson, W., & Golovich, N. 2019, RNAAS, 3, 58
McMillan, P. J. 2016, MNRAS, 465, 76
Mróz, P., Udalski, A., Skowron, J., et al. 2019, ApJS, 244, 29
Muraki, Y., Sumi, T., Abe, F., et al. 1999, PThPS, 133, 233
Navarro, J. F., Frenk, C. S., & White, S. D. M. 1996, ApJ, 462, 563
Penny, M. T., Gaudi, B. S., Kerins, E., et al. 2019, ApJS, 241, 3
Piffl, T., Scannapieco, C., Binney, J., et al. 2014, A&A, 562, A91
Press, W. H., Bellini, A., Teukolsky, S. A., Vetterling, W. T., & Flannery, B. P. 1988, Numerical Recipes: The Art of Scientific Computing (1st ed.; New York: Cambridge Univ. Press)
Raithel, C. A., Sukhbold, T., & Özel, F. 2018, ApJ, 856, 35
Robin, A. C., Reylé, C., Derrière, S., & Picaud, S. 2004, A&A, 416, 157
Rose, S., Lam, C. Y., Lu, J. R., et al. 2022, ApJ, 941, 116
Sanderson, R. E., Bellini, A., Casertano, S., et al. 2019, JATIS, 5, 044005
Sharma, S., Bland-Hawthorn, J., Johnston, K. V., & Binney, J. 2011, ApJ, 730, 3
Smith, M. C., Ruchti, G. R., Helmi, A., et al. 2007, MNRAS, 379, 755
Spergel, D., Gehrels, N., Baltay, C., et al. 2015, arXiv:1503.03757
Tisserand, P., Guillou, L. L., Afonso, C., et al. 2007, A&A, 469, 387
Udalski, A., Szymanski, M., Kaluzny, J., Kubiak, M., & Mateo, M. 1992, AcA, 42, 253
Udalski, A., Szymanski, M., Stanek, K. Z., et al. 1994, AcA, 44, 165
Udalski, A., Szymański, M. K., & Szymański, G. 2015, AcA, 65, 1
Wilson, R. F., Barclay, T., Powell, B. P., et al. 2023, ApJS, 269, 5
Wyrzykowski, L., Skowron, J., Kozłowski, S., et al. 2011, MNRAS, 416, 2949
Zel'dovich, Y. B., & Novikov, I. D. 1967, SvA, 10, 602